

# Crustal structure and Quaternary acceleration of deformation rates in central Washington revealed by stream profile inversion, potential field geophysics, and structural geology of the Yakima folds

Lydia Staisch<sup>1,2</sup>, Richard Blakely<sup>1</sup>, Harvey Kelsey<sup>3</sup>, Richard Styron<sup>4</sup>, Brian Sherrod<sup>2</sup>

<sup>1</sup> *U.S. Geological Survey, Geology, Minerals, Energy and Geophysics Science Center, Menlo Park, CA 94025*

<sup>2</sup> *U.S. Geological Survey, Earthquake Science Center, University of Washington, Seattle, WA 98195*

<sup>3</sup> *Department of Geology, Humboldt State University, Arcata, CA 95521*

<sup>4</sup> *Global Earthquake Model Foundation, Pavia, Italy, 27100*

## KEY POINTS

1. Deformation rates in the Yakima Canyon region accelerated in the Pleistocene
2. Faults that underlie the Yakima folds are reactivated and inverted normal faults
3. Slip rate estimates on individual faults suggest that large magnitude earthquakes may recur on hundred to thousand year timescales

This article has been accepted for publication and undergone full peer review but has not been through the copyediting, typesetting, pagination and proofreading process which may lead to differences between this version and the Version of Record. Please cite this article as doi: 10.1029/2017TC004916

## ABSTRACT

Post-Miocene tectonic uplift along fault-cored anticlines within central Washington produced the Yakima Fold Province (YFP), a region of active NNE-SSW shortening in the Cascadian backarc. The relative timing and rate of deformation along individual structures is coarsely defined yet imperative for seismic hazard assessment. In this work, we use geomorphic and geophysical mapping, stream profile inversion, and balanced cross section methods to constrain fault geometries and slip rates in the Yakima Canyon region. We extract stream profiles from LiDAR data and analytically solve for the rate of relative rock uplift along several active fault-cored anticlines. To constrain the fault geometries at depth and the long-term magnitude of deformation, we constructed two line-balanced cross sections across the folds with forward-modeled magnetic and gravity anomaly data.

Our stream profile results indicate an increase of incision rates in the Pleistocene, and we infer the increase is tectonically controlled. We estimate modern slip rates between 0.4 and 0.6 mm yr<sup>-1</sup> accommodated on reverse faults that core the Manastash Ridge, Umtanum Ridge, and Selah Butte anticlines and establish that these faults reactivate and invert older normal faults in basement rocks. Finally, we calculate the time required to accumulate sufficient strain energy for a large magnitude earthquake ( $M \geq 7$ ) along individual structures in the YFP. Results show that the Yakima folds likely accommodate large magnitude earthquakes and that it takes several hundred to several thousand years to accumulate sufficient strain energy for a  $M \geq 7$  earthquake.

## 1. INTRODUCTION

Directly measuring the evolution of tectonic uplift requires a landscape in which precisely datable geologic strain markers exist and are well distributed in time and space, a condition that is not always met. Fortunately, methods to extract and analyze the geomorphic signature of deformation have been developed over the past several decades and provide means to indirectly measure relative rock uplift and address outstanding tectonic questions about landscapes with limited geologic strain markers (Fox et al., 2014, 2015; Glotzbach, 2015; Goren et al., 2014; Whittaker et al., 2008). Fluvial networks adjust to topographic development primarily through channel steepening such that anomalously steep reaches along a channel long profile can be indicative of spatially or temporally varying rates of topographic growth (Kirby & Whipple, 2001, 2012; Snyder et al., 2000, 2003). Recent work has shown that even sparse direct measures of deformation rate can be used to calibrate observed changes in channel steepness to solve for the tempo of relative rock uplift and how it may change over time and space (Goren et al., 2014). Combined geomorphic and geologic measures of tectonic uplift are especially useful in regions of slow strain accumulation and poorly understood earthquake hazards where satellite measurements of active deformation are of limited resolution (Kirby et al., 2008).

The Yakima Fold Province (YFP), located in the backarc of the Cascadia subduction zone (Fig. 1), is a region of active seismicity related to deformation along an array of generally E-W to NW-SE trending fault-cored folds (Gomberg et al., 2012). Historical earthquakes in the region include the 1872 M6.8 Entiat and the 1936 M5.7 Milton-Freewater earthquakes (Bakun et al., 2002; Brown, 1937), in addition to low magnitude seismicity, typically  $M < 3$ . Geodetic data show  $\sim 2 \text{ mm yr}^{-1}$  of NNE-SSW shortening (McCaffrey et al., 2013, 2016), and while geodetic and earthquake data indicate active deformation, the slow strain environment of the YFP makes it difficult to assess the rate of deformation

accommodated on individual structures. Recent work using cosmogenic dating of strath terraces within the Yakima Canyon provides critical estimates of Quaternary relative rock uplift rates in the area and shows that recent deformation is focused along anticlinal ridges (Bender et al., 2016). Yet how these Quaternary deformation rates relate to decadal-scale and longer-term deformation is not well constrained. Furthermore, whether deformation along the Yakima folds involves deep crustal structures, and what those structures may be, remains debated (Casale & Pratt, 2015; Pratt, 2012; Reidel et al., 2013).

In this work, we acquire a continuous record of relative rock uplift rates and assess rates and magnitudes of long-term deformation along the three major structures of the Yakima Canyon: the Manastash Ridge, Umtanum Ridge, and Selah Butte anticlines (Fig. 1). In our geomorphic analyses, we exploit the availability of high-resolution LiDAR data and existing ages of strath terraces in the Yakima Canyon to invert stream profiles and analytically solve for relative rock uplift rates. We also construct and retrodeform two balanced cross sections, with additional constraints from gravity and high-resolution aeromagnetic anomaly data, to better understand the structure of the Yakima folds and provide a long-term geologic context for calculated relative rock uplift rates. Finally, we use the new slip rates and fault geometry to calculate the time required to accumulate sufficient strain energy for a large magnitude earthquake ( $M \geq 7$ ) along individual structures.

## **2. GEOLOGIC SETTING**

The Yakima Canyon is bounded in the north by the Kittitas Valley and in the south by the Selah Valley. Here, the Yakima River incised orthogonally through the Manastash Ridge, Umtanum Ridge, and Selah Butte anticlines, from north to south (Fig. 1). The Yakima Canyon has incised over 600 m through these folds and provides excellent exposure of the

typically north-vergent anticlines and occasionally overturned basaltic strata (Bentley, 1977; Kelsey et al., 2017) (Fig. 2).

The Miocene Columbia Flood Basalt Group (CRBG) is the most prominent rock type exposed in the Yakima Canyon and includes the Grande Ronde, Wanapum, and Saddle Mountains basalts, which are further divided into various flow members based on geochemical signature and paleomagnetic orientations (Figs. 1 and 3) (Barry et al., 2013; Camp, 1981; Reidel, 1983; Reidel et al., 2013; Reidel & Fecht, 1987; Swanson et al., 1979). While not exposed at the surface in the Yakima Canyon region, the stratigraphy of underlying units is fairly well defined from exploratory oil and gas wells (Fig. 1). Boreholes YM 1-33, BN 2-35, and SB-1 penetrate beneath the CRBG and into Oligocene volcanoclastic and clastic strata and Eocene clastic strata (Czajkowski et al., 2012). Only BN 2-35 penetrates into basement rock (Czajkowski et al., 2012). Strata that overlie the CRBG are exposed within the Kittitas and Selah valleys, but are largely absent from the deformed intervening region. These strata include the late Miocene – Pliocene upper Ellensburg Formation, the Pliocene Thorp Gravel, and Quaternary alluvium (Fig. 1).

Several sparse late Miocene – Quaternary strain markers exist and add important insight into recent deformation. The upper Ellensburg Formation (Smith, 1988a) and Thorp Gravel (Waite, 1979) are differentially tilted along the north-sloping forelimb of the Manastash Ridge anticline, and this relationship has been used to argue for post-Pliocene deformation (Bentley, 1977; Bender et al., 2016). In addition, the Thorp Gravels were deposited and are exposed along the flanks of the Umtanum Ridge anticline (Schuster, 1994) and uplifted several hundred meters relative to correlative deposits in the Kittitas and Selah valleys. Finally, strath terraces within the Yakima Canyon have been recently dated between 0.1 and 1.6 Ma and indicate that Quaternary incision rates are higher along anticlinal crests than in synclinal troughs (Bender et al., 2016). While the upper Ellensburg Formation, Thorp

Gravel, and dated strath terraces suggest post-Pliocene to Quaternary deformation along the Yakima folds, these geologic markers only provide a rough estimate of deformation rates and how they may have changed over time.

### 3. STREAM PROFILE INVERSION

Mathematical river incision models are often used to quantify relative rates of landscape evolution, where local channel steepness is set by relative rock uplift rate, bedrock erodibility, and climatic variability (Whipple et al., 2000). In regions of spatially and temporally uniform bedrock and climate, channel steepness is proportional to rock uplift rates, allowing for indirect calculation of tectonic and erosion rates from elevation models. Most widely accepted models are typically based on the stream power incision model of Howard & Kerby (1983):

$$E = KA^m S^n \quad (1)$$

where  $E$  is the incision rate,  $K$  is the erodibility constant dependent on process-oriented, climatic, and geologic factors (Whipple, 2004),  $A$  is upstream drainage area,  $S$  is local topographic slope, and  $m$  and  $n$  are positive exponents. Combined with the detachment-limited mass balance equation (Howard, 1994; Howard & Kerby, 1983) equation 1 becomes:

$$\frac{dz}{dt} = U - E = U - KA^m S^n \quad (2)$$

where the change in elevation along a stream over time ( $dz/dt$ ) is the result of relative rates of rock uplift ( $U$ ) and river incision ( $E$ ), with respect to base level. Under topographic steady state ( $E = U$ ), we can relate local gradient ( $S$ ) to relative rock uplift rate ( $U$ ) (Flint, 1974; Hack, 1957; Kirby & Whipple, 2012):

$$S = \left(\frac{U}{K}\right)^{1/n} A^{-m/n}. \quad (3)$$

This equation provides the fundamental link between channel slope and rock uplift rate, which may vary either spatially or temporally. In regions where abrupt changes in channel steepness (knickpoints) do not spatially correlate to tectonic structures or lithologic contacts, such as the Yakima folds (Fig. 4), channel morphology may record temporal variations in relative rock uplift rate. In this case of a transient landscape, the lower reaches of a stream are equilibrated to the modern rate of uplift, whereas the upper reaches are equilibrated to the previous rate of uplift (Whipple & Tucker, 1999); with time, the transition point between the two equilibria migrates upstream. To estimate at what point in time rate changes may have occurred, we use the equation for channel response time ( $\tau$ ) to tectonic perturbations (Whipple and Tucker, 1999; Goren et al., 2014), where  $\tau(x)$  is the response time for perturbations to propagate from the river outlet at  $x=0$  to a point  $x$  along the channel:

$$\tau(x) = \int_0^x \frac{dx'}{KA(x)^m S(x)^{n-1}}. \quad (4)$$

The near uniform basaltic bedrock of central Washington and homogenously semi-arid climate make the Yakima folds an ideal landscape to extract elevation data for uplift rate estimation (Figs. 1 and S1-S2). Additionally, while the geomorphology of central and eastern Washington was significantly altered during Pleistocene outburst floods from glacial Lake Missoula, the Yakima Canyon was sheltered (Benito & O'Connor, 2003; Bretz, 1925; 1932; Smith, 1993; Waite, 1980, 1985) and therefore older landforms are sufficiently well preserved for analysis. To solve for relative rock uplift rate over time, we invert the equation:

$$z(0, x) = \int_{-\tau(x)}^0 U(t') dt' \quad (5)$$

for block uplift from Goren et al. (2014), where the rate of rock uplift is determined from the measured values of elevation ( $z$ ), slope ( $S$ ), area ( $A$ ), and distance ( $x$ ) along a longitudinal profile. Slope and area are incorporated in the lower limit of the integrand ( $\tau(x)$ , Equation 4).

Measured geomorphic values ( $z$ ,  $S$ ,  $A$ ,  $x$ ) come from 2-m LiDAR topography extracted along streams that drain three tectonic structures: the Manastash Ridge, Umtanum Ridge, and Selah Butte anticlines (Fig. 4B).

We limit our analysis to streams that drain topography produced by each structure and to areas that have not been significantly altered by agriculture or road construction, since these human activities influence and complicate digital elevation models and extracted stream data (Fig. 4B). We must therefore exclude streams that drain into the Kittitas or Selah valleys prior to confluence with the Yakima River. We also exclude the streams that drain the north-facing slopes of the Umtanum Ridge because they cross the major fault trace between the Umtanum Ridge and Manastash Ridge fault blocks (Fig. 4B). From the morphology and glacial history of the region, we confirm that Pleistocene glaciers did not extend into the catchments analyzed (Porter, 1976). For the preceding and following equations, we make the common assumption of a linear solution to the stream power law ( $n=1$ ) (Goren et al., 2014).

To infer relative rock uplift rate from the topographic dataset, we calibrate several parameters to the landscape, namely the area exponent ( $m$ ) and the erodibility constant ( $K$ ) for the transient stream power model. Both of these parameters strongly influence the results of calculated relative rock uplift rate ( $U$ ) and channel response time ( $\tau$ ). Additionally we must select the number of time interval,  $q$ , and smoothing factor,  $L$ , that sufficiently capture the rate and change of relative rock uplift without oversimplifying our dataset or allowing data artifacts to propagate into unrealistic models (Goren et al., 2014; Fox et al., 2015).

### **3.1. Calibration of the Erodibility Constant, Area Exponent**

Empirical studies find that channel steepness ( $k_s$ ) along a stream profile can be calculated using power-law scaling relationship between drainage area and local slope (Flint, 1974; Hack, 1957; Howard & Kerby, 1983). When combined with the stream power incision model (Equation 1) this becomes:



$$k_s = SA^{m/n} = \left(\frac{E}{K}\right)^{1/n}. \quad (6)$$

The relationship above allows calibration of the erodibility constant ( $K$ ) with measurements of incision ( $E$ ) and steepness ( $k_s$ ) (DeLong et al., 2017; Kirby & Whipple, 2001; Whipple, 2004). For the Yakima Canyon, we used incision rates from cosmogenic nuclide dating of strath surfaces (Bender et al., 2016) and measurements of normalized channel steepness from a 2-m resolution LiDAR dataset following the procedure outlined by Wobus et al., (2006). We estimate  $K$  to be  $7.08\text{E}-06 \pm 9.98\text{E}-07 \text{ m}^{0.2} \text{ yr}^{-1}$  by calculating the likelihood of the linear regression fit to the 2-sigma uncertainty in the measured data, with a reference concavity  $\theta=0.4$  (Fig. 5). The likelihood of each regression was computed based on the assumption that uncertainties of the measured data are Gaussian. The linear regression trials were sampled from the posterior to return a normalized relative probability distribution for slope and intercept values. We use the linear fit with the highest calculated likelihood as our best-fit estimate of  $K$  and uncertainty in  $K$  was determined from the 95% confidence interval of the sampled posteriors.. The Yakima folds are hosted uniformly in basalt, thus we justify using a uniform value of  $K$  for further calculations. We note that  $K$  was estimated from the Yakima River, where  $k_s n$  values are relatively low, between 6 and 14, whereas  $k_s n$  values in tributaries are steeper (Fig. 4). The uncertainty in  $K$  is used to estimate the uncertainty in  $U$  and  $\tau$ . Since channel response time is integrative over stream length, the uncertainty in channel response time increases towards the headwaters.

To define a suitable value of the area exponent ( $m$ ), we use  $\chi$ -plot methods (Perron & Royden, 2013) and assume that profiles are in equilibrium and exponent  $n=1$  (see above). This method normalizes streams by a reference drainage area and concavity, thus removing the influence of drainage area on the longitudinal slope profile. The linearization of stream profiles by transforming the distance coordinate,  $x$ , to the area-independent value,  $\chi$ , is an

improvement on the conventional slope-area analysis for finding the value of  $m$  (Perron & Royden, 2013). We obtain the best-fit exponent value by maximizing the linear fit of streams in  $\chi$ - $z$  space (Fig. 6). For our streams, this has the same result as the method of minimizing misfit between trunk streams and tributaries of all extracted stream profiles (Goren et al., 2014). We find that the best-fit area exponent value ( $m$ ) is 0.4 (Fig. 6).

### 3.2. Linear Least Squares Solution for Block Uplift Conditions

With  $m$  and  $K$  estimated, we define vectors  $\mathbf{z}$  and  $\boldsymbol{\tau}$  to be the elevations at each pixel in our stream extracted stream networks and corresponding values of  $\tau$  calculated using Equation 5. This allows us to estimate the relative rock uplift rate value ( $U$ ) at each point in the stream network using the block uplift end member least squares inversion developed by Goren et al. (2014), in which the integral expression for relative rock uplift rate is discretized into time intervals ( $\Delta\tau$ ). The elevation at each point ( $z_i$ ) can be estimated by:

$$\mathbf{A}\mathbf{u} = \mathbf{z} \quad (7)$$

where

$$\mathbf{z} = [z_1 \ z_2 \ \dots \ z_i \ \dots \ z_N] \text{ and } \mathbf{u} = [u_1 \ u_2 \ \dots \ u_j \ \dots \ u_q]. \quad (8)$$

Matrix  $\mathbf{A}$  is an  $N \times q$  matrix,  $N$  is the number of data points and  $q$  is the number of discrete time intervals and each row of matrix  $\mathbf{A}$  sums to  $\tau_i$ . As an initial estimate of relative rock uplift rate, we use every data point in the stream channels, such that  $N = q$ . However, given the high resolution of the topographic dataset, there are more data points from the 2-m LiDAR topographic dataset than discrete changes in relative rock uplift rate. Topographic data are often smoothed or damped in order to avoid small errors or data artifacts propagating into large errors in estimated relative rock uplift rate (Goren et al., 2014; Fox et al., 2015). Thus we apply a zero-phase moving average to smooth the elevation vector  $\mathbf{z}$  and apply a linear least squares scheme to estimate  $\mathbf{u}$ :

$$\mathbf{u} = (\mathbf{A}^T \mathbf{A} + \mathbf{I})^{-1} \mathbf{A}^T \mathbf{z}^S \quad (9)$$

where  $\mathbf{z}^S$  is the  $N$ -length vector with smoothed elevation values and  $\mathbf{I}$  is a small  $q \times q$  identity matrix. We repeat this inversion with various values of  $L$  and  $q$  and calculate the predicted elevations for the resulting inferred relative rock uplift history. For each combination of  $L$  and  $q$ , we calculate the misfit between measured and predicted elevations using equation:

$$misfit = \frac{1}{N-q} \sqrt{\sum_{i=1}^N (z_i - z_i^{pred})^2} \quad (9)$$

where  $z_i$  and  $z_i^{pred}$  are the measured and predicted elevation values, respectively. We select the number of time interval,  $q$ , and smoothing factor,  $L$ , that minimize misfit while maximizing smoothing (Fig. S3). Our results show that for  $q = 30, 50, 70$ , and  $90$ , the optimal smoothing factor is  $600$ . To gain confidence in the inferred rock uplift histories, Goren et al. (2014) designed a temporal resolution study in which they imposed a hypothetical uplift history and forward modeled three synthetic topographic profiles with (1) no added noise, (2)  $\pm 10$  m white noise, or (3)  $\pm 100$  m white noise. The imposed uplift history is then compared to the inferred uplift history from linear least squares of the synthetic topographies, allowing one to identify whether or not the chosen smoothing ( $L$ ) and time interval ( $q$ ) reproduce reasonable results. We adopted this analysis with the real  $\tau$  distribution from Yakima Canyon LiDAR data. Results show good agreement between imposed and inferred relative rock uplift histories for  $q$  values between  $30$  and  $70$  and  $L=600$ . Some small artifacts were identified in all trials with  $\pm 100$  m white noise (Fig. S4). We calculated misfit between the imposed and inferred topographic data and found that  $L=600$  and  $q=50$  produce the best results (Fig. S4). We therefore adopt these values for inferring the relative rock uplift history of the Manastash Ridge, Umtanum Ridge, and Selah Butte anticlines.

### 3.3. Results

Stream profile inversion results for three individual fault-cored folds show a common pattern of acceleration in incision rate in Pleistocene time with high rates maintained through Quaternary time (Fig. 7). All modeled incision rates are relative to modern Yakima River base level. Modeled relative rock uplift rates for the northernmost fold, Manastash Ridge anticline, are calculated for the past  $6.1^{+1.1}_{-0.7}$  Ma (Fig. 7A). Our results reveal slow rates, below  $0.1 \text{ mm yr}^{-1}$ , until  $\sim 1.3$  Ma (Fig. 7A). After this time, relative rock uplift rates increase to  $0.14 - 0.20 \text{ mm yr}^{-1}$  (Fig. 7A). We calculate  $0.40 \pm 0.09 \text{ km}$  cumulative relative rock uplift for the Manastash Ridge anticline by summation of modeled rates multiplied by each time step (Fig. 7B).

Similarly, modeled relative rock uplift rates for the Umtanum Ridge anticline calculated over the past  $6.2^{+1.0}_{-0.7}$  Ma are initially slow, below  $0.1 \text{ mm yr}^{-1}$  (Fig. 7C). Relative rock uplift rates peak to  $0.11 - 0.22 \text{ mm yr}^{-1}$  between Pleistocene and modern time (Fig. 7C). The acceleration in relative rock uplift rate along the Umtanum Ridge anticline is somewhat more gradual than for the Manastash Ridge anticline (Figs. 7A and 7C). The cumulative relative rock uplift calculated for the Umtanum Ridge anticline is  $0.63 \pm 0.11 \text{ km}$  (Fig. 7D).

The calculated relative rock uplift rates for the Selah Butte anticline are over a shorter time period, owing to the shorter streams used for inversion (Fig. 4B). Results show a gradual increase in relative rock uplift rate starting at  $\sim 2.2$  Ma, with peak rates at  $\sim 0.23 \text{ mm yr}^{-1}$  between 0.5 and 0.6 Ma (Fig. 7E). We calculate that the Selah Butte anticline has accommodated  $\sim 0.30 \text{ km}$  of rock uplift since  $\sim 2.2$  Ma (Fig. 7F).

### 3.3. Comparison with Paleoclimate Data, the Uplifted Thorp Gravel, and Yakima River Strath Terraces

Isotope data from Miocene – Holocene pedogenic carbonates and hydrated glass indicate a progressive decrease in annual precipitation in eastern and central Washington, suggesting coincident topographic uplift of the Cascade Range and desertification of the backarc (Takeuchi & Larson, 2005; Takeuchi et al., 2010). The expected effect of this change in mean annual precipitation on the erosive power and incision rates of rivers in the Cascadia backarc is exactly opposite to the steepening and increased relative rock uplift determined from stream profile inversion. We therefore suggest that changes in climate are unable to explain modeled incision rates along the Yakima folds, and therefore infer that modeled incision rates are predominantly set by tectonically driven relative rock uplift.

The Thorp Gravel is an important young strain marker in the Yakima Fold Province that test our inference that modeled incision rates are driven by tectonic uplift. These continental gravels were deposited ca. 2.9 Ma in an alluvial setting and graded to the late Miocene – Pliocene Yakima River (Bender et al., 2016), in agreement with the maximum depositional ages ( $3.6 \pm 0.4$ ) from detrital zircon fission track (Waitt, 1979). Clast compositions of the Thorp Gravel range from predominantly Cascade-derived volcanic andesites and basaltic andesites to predominantly Columbia River basalt clasts depending on proximity to the Cascade Range. In the Kittitas Valley, north of the Yakima River Canyon, Thorp Gravel deposits are found at modern elevations of 440 – 465 m (Fig. 8). Similarly, Thorp Gravel exposures in the Selah Valley, located south of the Yakima River Canyon, are at 435 – 470 m (Fig. 8). The overlap in deposit elevations suggests that little differential uplift and incision has occurred in the Kittitas Valley relative to the Selah Valley. In contrast, Thorp Gravel deposits within the Selah Creek drainage, on the flanks of the Umtanum Ridge

anticline, occur at elevations between 670 – 750 m (Fig. 8), suggesting that there has been between 230 – 280 m of uplift along the Umtanum Ridge anticline since  $2.9 \pm 0.1$  Ma.

The cumulative uplift we calculate from stream profile inversion along the Umtanum Ridge anticline since 2.9 Ma is  $315 \pm 70$  m (Fig. 7D), with the Yakima River set as base level. The Yakima River has incised the Yakima and Kittitas Valleys ~50 m since Thorp deposition; thus the modeled post Miocene tectonic uplift of the Thorp Gravel along the Umtanum Ridge anticline is slightly reduced to  $265 \pm 70$  m. The consistency in calculated and measured cumulative deformation inferred from Thorp Gravel deposits suggests that our modeled uplift rates are accurate. By using the Yakima River as base level, our modeled relative rock uplift rates include a  $0.01 \text{ mm yr}^{-1}$  component of fluvial incision. Accordingly, to calculate tectonic rock uplift rates, we reduce our modeled rates by  $0.01 \text{ mm yr}^{-1}$  (Table 2).

The Yakima River incises orthogonal to the main strike of fold structures, and thus the recent cosmogenic dating of Yakima River strath terraces provides additional insight into rates of river incision and tectonic uplift (Bender et al., 2016). Incision rates inferred from strath terrace measurements are highest near anticlinal ridges and towards frontal faults (Fig. 8). While the measured incision rates from terraces are time-integrated, the  $10^5$  timescale over which the youngest strath terraces dated by Bender et al. (2016) have averaged incision rates appears to be relatively constant and can therefore be directly compared to our incision rate estimates. We also note that the incision rates measured by Bender et al. (2016) are used to estimate the erodibility constant ( $K$ ); as such the comparison between model results and measured incision rates may seem circular, however we note that the streams used for inversion have smaller drainage areas than the Yakima River. Therefore, the comparison between measured and modeled incision rates is an internal check that our estimated values of  $K$  from Yakima River strath terraces are applicable for smaller tributary streams.

The ~0.2 Ma strath terrace closest to the Manastash Ridge anticlinal crest suggests that the Yakima River is incising at a rate of  $0.114^{+164}_{-79}$  mm yr<sup>-1</sup> (Bender et al., 2016), within uncertainty of our estimates from stream profile inversion (Fig. 7A). Similarly, measured incision rate for the 0.1 Ma strath terrace near the Umtanum Ridge anticlinal crest is >0.07 mm yr<sup>-1</sup>, in agreement with calculated relative rock uplift rates from stream profile inversion (Fig. 7C) (Bender et al., 2016). The 1.6 Ma Meander strath terrace site, located between the Umtanum and Manastash ridges, and Thorp Gravel site in Kittitas Valley have comparably low incision rates (Bender et al., 2016), suggesting the intervening syncline has experienced little to no uplift relative to the Kittitas and Selah valleys. These spatially variable rates along the Yakima River indicate that uplift due to compressive deformation is concentrated near the fold and fault traces, whereas incision near synclinal troughs largely reflects regional fluvial incision (Bender et al., 2016).

#### **4. FAULT GEOMETRY AND CUMULATIVE DEFORMATION**

We constructed two balanced cross sections from Kittitas Valley southward to the Selah Valley to constrain the magnitude of post-CRBG shortening and fault geometries at depth. Cross section A-A' was designed to assess total shortening across the canyon region given its proximity to abundant structural measurements. The transect is 27 km in length and oriented at N21°E, the inferred direction of maximum convergence (Fig. 3). Cross section B-B' was designed to capture the structural relationships between Umtanum Ridge and Selah Butte anticlines, is 20 km in length, and is parallel to A-A' (Fig. 3). Our structural analyses and interpretations are guided by existing geologic mapping at 1:100k scale (Schuster, 1994; Walsh, 1986), with bedding orientations supplemented from (Miller, 2014), existing structural cross sections of Manastash Ridge anticline (Kelsey et al., 2017), stratigraphy from

exploration borehole logs (Czajkowski et al., 2012), and forward modeling of aeromagnetic and gravity data (Figs. 3 and 9).

#### **4.1. Structural Geology and Stratigraphy**

We used the mapped structures and established stratigraphy of the Yakima folds as the primary geologic data for constraining the magnitude of deformation and fault geometries at depth (Fig. 3). The Manastash Ridge and Umtanum Ridge anticlines are north-vergent fault-cored folds, in which the main south-dipping reverse faults and associated backthrusts accommodate NE-SW oriented shortening (Fig. 3). The Selah Butte anticline is a relatively short (~20 km long) structure mapped as south-vergent and possibly related to the Umtanum Ridge anticline (Fig. 3).

The majority of rock exposed within the YFP is the Miocene Columbia River Basalt Group. Over a broad scale (100's of km), the thicknesses of the CRBG flows can vary, however thickness remains relatively consistent at a more local scale (10's of km) along our cross section transects. Proximal boreholes provide insight into the underlying regional stratigraphy of the Yakima folds. Boreholes SB-1, YM 1-33 and BN 2-35 penetrate through the Miocene CRBG and into the Eocene to Oligocene clastic and volcanoclastic strata, which include the Wildcat Creek, Ohanapecosh, Roslyn, and Swauk Formations (Fig. 10C) (Czajkowski et al., 2012). Borehole SB-1 is the only borehole to encounter granitic basement rock, possibly the Cretaceous Mount Stuart Batholith, at depth (Wilson et al., 2008).

#### **4.2. Potential Field Data**

Gravity anomaly and high-resolution aeromagnetic data available for the study region further constrain the geometry of structures and composition of the upper to middle crust in the Yakima Canyon region. The U.S. Geological Survey acquired two aeromagnetic surveys in 2008 and 2009. The International Geomagnetic Reference Field, updated to the time of flight, was subtracted from original total-field measurements to produce the 100-m resolution



total-field magnetic anomaly map in Figure 9A. In this map, the wavelength and steepness of horizontal magnetic gradients is well correlated with Yakima fold structures (Fig. 9A), facilitated by the large variability in magnetic characteristics of the Columbia River Basalt Group that regionally composes the upper several kilometers of the crust. The gravity database is derived from various sources, including proprietary data from hydrocarbon exploration and published data from Finn et al. (1991). The isostatic residual gravity anomaly map in Figure 9B was produced by reducing gravity measurements using standard procedures (Blakely, 1995). Regional gravity anomaly trends in central Washington show that strong positive anomalies overlie exposures of pre-Tertiary bedrock, such as the Mount Stuart Batholith and the Ingalls Tectonic Complex (Blakely et al., 2011; Dragovich et al., 2002).

We extracted gravity and magnetic anomaly values along each transect to assist in our construction of balanced cross sections. Forward modeling was completed by developing hypothetical crustal sections that were fit by trial-and-error to the observed potential-field data and constrained by surface geologic information and borehole data (Figs. 9 and 10). Gravity and magnetic data add strong constraints on viable cross sections. For example, the upper basaltic crust is strongly magnetic and has layers of both normal and reverse magnetic polarity, whereas underlying rocks are less magnetic (Blakely et al., 2011). Thus, magnetic anomalies are particularly sensitive to upper crustal structure of the Yakima folds. On the other hand, gravity anomalies are strongly affected by density contrasts between basalt, sedimentary strata, and basement rocks. Thus, gravity modeling results are sensitive to changes in basement topography, as well as upper crustal structure. For our models, we use magnetic and density parameters similar to Blakely et al. (2011) (Table 1).

#### **4.3. Balanced Cross Section Results**

Forward modeling of the magnetic and gravity anomaly data show excellent agreement with measured potential field data (Figs. 10A-B and 10E-F), with the exception of

Yakima Canyon, where the magnetic anomaly transect crosses a region of focused incision (Fig. 10A). Over the Yakima Canyon, the pilot was forced to fly higher above ground than elsewhere, resulting in smoother magnetic anomalies over the canyon.

The resulting balanced cross sections are shown in Figures 10C and 10G, and a wider cross section, which shows the full width of modeled basement topography, is shown in Figure 10D. We find that significant basement topography is required to match the measured gravity anomaly data (Fig. 10B), similar to the findings by Blakely et al. (2011). We also find that the Selah Butte anticline is formed from motion along the same fault that soles beneath the Umtanum Ridge anticline, from which we infer that Selah Butte was caused by a backthrust rooted in the Umtanum thrust fault (Fig. 10G).

We retrodeformed cross section A-A' to find an original length of 30.4 km, which indicates that the Yakima Canyon region has been shortened by ~3.5 km (11.5%) since the mid-Miocene (Figs. 10 and S4). The majority of shortening has been accommodated along the Umtanum Ridge anticline and its underlying fault, which together accommodate ~2.4 km shortening. The Manastash Ridge anticline and its associated reverse and backthrust faults accommodate the remaining ~1.1 km shortening. The amount of reverse dip-slip displacement accommodated in Miocene strata along the main thrust fault beneath Umtanum Ridge is ~2.42 km, whereas the main fault beneath Manastash Ridge accommodates only ~0.57 km of reverse dip-slip displacement in Miocene strata. Retrodeformation of post-mid Miocene deformation (Fig. S5) reveals that ~1.83 km of reverse dip-slip displacement was accommodated along the Manastash Ridge prior to eruption of the CRBG, indicating that this structure accommodated shortening between Eocene and Miocene time. In contrast, we do not find significant pre-Miocene shortening along the main thrust fault beneath Umtanum Ridge.

While post-Eocene deformation along cross section A-A' is characterized by shortening and reverse faulting, the basement topography is suggestive of a prior history of normal faulting (Fig. 10D). We therefore interpret that the structures of the Yakima Canyon initiated as normal faults and have been reactivated as reverse faults sometime between Eocene and Miocene time. After emplacement of the CRBG, the faults propagated up-section.

The interpretation of reverse faults soling into inverted normal faults at depth is not a requirement of our gravity modeling, but the interpretation is the most geologically consistent with independent tectonic interpretations. Along what is now the western margin of the North Cascade mountains, and only 60-120 km to the west and northwest of cross section A-A', Eocene clastic basin deposits and the northeast-trending Teanaway dikes were emplaced within an overall transtensional environment (Doran, 2006; Eddy et al., 2016; Evans & Johnson, 1989; Evans, 1994; Johnson, 1985; Mendoza, 2008; Miller et al., 2009; Tabor et al., 1984). Because Eocene faults in the Yakima canyon area are proximal to the above transtensional setting, it is reasonable to infer an extensional setting of the Eocene-age Yakima canyon faults as well.

Located 13 km to the east, cross section B-B' is restored to an original length of 21.6 km, suggesting only 1.6 km (7.6%) of shortening along this section of the Umtanum Ridge-Selah Butte fault system. At depth, we find that the total amount of dip-slip displacement along cross section B-B' is 2.34 km. Above 1 km depth, dip-slip displacement is distributed along one main thrust fault (~1.0 km) and three backthrust faults (collectively 1.3 km). The total amount of shortening and dip-slip motion reconstructed along the faults that core the Umtanum Ridge and Selah Butte anticlines from cross section B-B' is comparable to the 2.42 km reconstructed along A-A'. The basement topography modeled in cross section B-B' is similar to that of A-A' but with basement highs shifted slightly to the south. This suggests

that basement structures may have a generally NW-SE trend, as apparent in gravity anomaly data (Fig. 9B).

#### **4.4. Comparison of Cross Section and Stream Profile Results**

Balanced cross sections and stream profile analyses provide independent estimates of vertical rock uplift along individual structures in the Yakima Canyon. Stream profile results are a measure of rock uplift relative to the Yakima River, so we must use the same base level in our comparison with cross section results. The cumulative relative rock uplift since  $\sim 6.3 - 6.4$  Ma from stream profile inversion along the Manastash and Umtanum Ridges is  $0.48 \pm 0.09$  and  $0.66 \pm 0.09$  km, respectively (Table 2). From cross section A-A', we estimate maximum rock uplift along the Manastash and Umtanum ridge anticlinal crests, with the Yakima River as base level, at 0.50 and 0.66 km (Table 2). Along cross section B-B', it is difficult to differentiate between rock uplift along the Selah Butte and Umtanum Ridge anticlines because they sole into a common fault at depth. We therefore only use the estimate of maximum relative rock uplift along the main fault at 0.65 km (Table 2). The estimates of rock uplift from both cross sections closely match results from stream profile inversion, indicating that the stream profiles capture the majority of deformation accommodated within the Yakima Canyon region.

### **5. EARTHQUAKE HAZARD ASSESSMENT OF THE YAKIMA FOLDS**

We calculated the slip rates along the faults that core the Manastash and Umtanum Ridge anticlines using simple trigonometric relationships between the fault dip angle from our balanced cross sections and relative rock uplift rates averaged over the past 100 kyr from stream profile inversion results (Table 2). We used the new slip rate estimates and fault geometries for the faults that core the Manastash and Umtanum Ridge anticlines to calculate the time required to accumulate sufficient strain energy along faults for seismic rupture. The

equations used to calculate earthquake interevent times, which are a transformation of the definition of seismic moment, are identical to the methods described in Staisch et al. (2017).

Our calculations show that earthquakes of moderate magnitude, between  $M5 - M6.5$ , could recur on annual to centennial timescales; earthquakes of large magnitude ( $M7 - M7.5$ ) could recur on  $10^2 - 10^4$  timescales (Fig. 11; Table 3). The fault beneath Umtanum Ridge is most concerning because of its length and higher slip rate. It has the possibility of producing large magnitude earthquakes as often as every  $\sim 200$  years. The interevent times reported here (Fig. 11; Table 3) are directly comparable to the interevent times for a neighboring Yakima fold structure, the Saddle Mountains fault (Staisch et al., 2017). Our interpretations of these results as a proxy for earthquake recurrence interval rest on several important assumptions. First, we assume that all strain energy accumulated on the entire fault plane is released during an earthquake (i.e. no aseismic strain release). Second, we assume that all of the strain accumulated is released during an earthquake.

## **6. DISCUSSION**

### **6.1. Summary of the tectonic history of the Yakima Canyon**

Together, geologic, geomorphic, and geophysical data allow us to reconstruct the structural and topographic history of the Manastash Ridge, Umtanum Ridge, and Selah Butte anticlines of the Yakima Fold province. The faults that core these anticlinal ridges have a long history of deformation, originating as normal faults that offset dense basement rocks (Fig. 10D). The onset of normal fault motion is not well constrained; however interpretation of Eocene clastic strata and basaltic dikes suggest that extension transtension was ongoing in Eocene time (Doran, 2006, 2006; Eddy et al., 2016; Evans & Johnson, 1989; Evans, 1994; Johnson, 1985; Mendoza, 2008; Miller et al., 2009; Tabor et al., 1984). Both Oligocene and Eocene clastic and volcanoclastic strata are offset by reverse motion (Fig. 10D), indicating

that normal faults were inverted either during or after the Oligocene. The major erosional unconformity between the CRBG and pre-Miocene strata (Fig. S5) suggests a lull in deformation that we posit to occur after deposition and initial shortening of Oligocene strata and continued at least up to the time of initial emplacement of the CRBG, similar to the tectonic history inferred for the neighboring Saddle Mountains anticline (Casale and Pratt, 2015).

Structural offset along the faults that core the Manastash and Umtanum Ridges may have occurred during mid-Miocene eruption of the CRBG (Reidel et al., 1989), however deformation was not sufficient to divert the course of the Miocene ancestral Yakima River (Smith, 1988b). Furthermore, our data indicate that the majority of structural deformation and topographic growth along the Yakima Canyon anticlines took place after ~6.3 – 6.4 Ma during the waning stages of CRBG volcanism (Barry et al., 2013; Reidel et al., 2013). Our stream profile inversion results suggest that relative rock uplift of the Yakima folds was fairly slow and steady until late Miocene – early Pleistocene time. Tectonic uplift of both the Umtanum and Manastash ridge anticlines accelerated ca. 2.0-1.5 Ma, with increased rates of rock uplift sustained to the present.

We also investigated the possibility that the post-16 Ma growth of the north-trending Hog Ranch-Naneum anticline (Kelsey et al., 2017), the fold hinge of which trends through the east end of the profiled streams (Fig. 4A), affected the profile inversion results. In a comparison of streams east of the Yakima River and west of the Yakima River, we did not see a notable difference in relative rock uplift rate history derived from inversion results. The lack of a difference is not necessarily indicative of inactivity of the Hog Ranch-Naneum anticline, but rather that base level drop of Yakima River relative to the profiled streams is more directly affected by contraction along the three investigated Yakima folds.

## 6.2. Pliocene tectonic mechanisms to induce accelerated backarc deformation rates

While we find an increase in the rate of deformation within the Yakima Canyon region, it remains unclear whether deformation rates increased throughout the YFP. Recent analysis of the Miocene – Pliocene Ringold Formation suggests that relative rock uplift rates along the Saddle Mountains anticline increased five-fold since late Miocene time (Staisch et al., 2017). However, long-term rotation rates from paleomagnetic data and geodetic rotations rates indicate that deformation has remained fairly consistent since 16 Ma (Wells & McCaffrey, 2013; Wells et al., 1998). The somewhat contradictory data lead us to ask whether any event occurred in late Miocene to Pliocene time that could potentially affect shortening rates in the Cascadia backarc.

Assuming north-south shortening rates did increase regionally in late Miocene – Pliocene time, the increase may relate to changes along the Cascadia convergent plate margin. An acceleration in shortening in the overriding plate could result from an increase in the rate of convergence between stable North America and the subducting Juan de Fuca plate, an increase in the obliquity of convergence, or an increase in slip partitioning resolved along the subducting slab (McCaffrey, 1992, 2002). As the Juan de Fuca plate is consumed beneath the North American plate, the actively subducting oceanic crust becomes younger, more thermally buoyant, and more likely to resist subduction. We therefore suggest that an acceleration in plate convergence is improbable, but rather a deceleration of convergence is expected (Riddihough, 1984).

According to instantaneous rotational poles calculated from seafloor magnetic anomalies, the Pliocene was a time of change for the Juan de Fuca plate system. Between 3 and 4 Ma, the Explorer plate began to subduct independently from the Juan de Fuca plate, initiating a slab tear along the proposed Nootka fault (Audet et al., 2008; Hyndman et al., 1979; Riddihough, 1984; Rohr & Furlong, 1995). Geochemical data from the Garibaldi

Volcanic Belt support the existence of a slab tear between the buoyant Explorer plate and more steeply subducting Juan de Fuca plate, where trace element compositions are suggestive of a northward increase in the contribution of a primitive asthenospheric melt source (Mullen & Weis, 2015).

The detachment of the buoyant northern Explorer plate changed the orientation of Juan de Fuca plate subduction between 3 and 4 Ma, which later stabilized after about 2.4 Ma (Nishimura et al., 1984). The change in orientation may have modified the stresses accommodated along the subduction margin and/or in the overriding crustal blocks. Additionally, the induced toroidal flow in the mantle around the edge of the Pliocene slab tear, resolved as trench parallel southward flow across the Juan de Fuca slab, may inhibit the northward component of oblique subduction accommodated along the subduction interface (Fig. 12). The suppression of trench parallel convergence would therefore increase the strain partitioning along the Juan de Fuca plate margin and transfer trench-parallel strain into the overriding crustal blocks (McCaffrey, 1992, 2002). Indeed, analysis of shear wave splitting indicates that trench-normal stresses are only dominant in the overriding plate near the locked portion of the Cascadia subduction zone, with the majority of the forearc exhibiting a trench-parallel maximum compressional direction (Currie et al., 2001). Whether toroidal flow was induced directly after the Explorer plate detached from the Juan de Fuca plate or initiated later in time is unclear. However, both the change in orientation of subduction and the onset of southward asthenospheric flow across the subducting Juan de Fuca slab provide possible mechanisms for Pleistocene acceleration of north-south shortening in the backarc of the Cascadia subduction zone.



## 7. CONCLUSIONS

In this work, we show that the analyses of geomorphic, geologic, and geophysical datasets provide independent and complementary estimates of deformation in the Yakima Canyon region of the YFP. We find that crustal shortening accommodated after ca. 6.3 – 6.4 Ma generated the majority of the constructional topography along the Manastash Ridge, Umtanum Ridge, and Selah Butte anticlines. The long-term deformation along structures within the YFP penetrates to depths of 10 km or greater and is not limited to Neogene time. We interpret modeled potential field data and balanced cross section results to suggest that extension was accommodated along faults that penetrate basement rock until Eocene time. Faults were later inverted to accommodate crustal shortening at some time prior to eruption of the CRBG.

From stream profile inversion, we find that the rate of deformation along the Yakima folds has varied over time. Stream profile results show a notable acceleration in deformation in Pleistocene time. Deformation rates have remained elevated since the Pleistocene, with near-modern slip rates estimated at 0.4 and 0.6 mm yr<sup>-1</sup> along the faults underlying the Manastash and Umtanum Ridge anticlines, respectively. We suggest that the Pliocene slab tear between the Juan de Fuca and Explorer plates, considered to induce toroidal flow and southward migration of asthenospheric material across the Juan de Fuca slab (Fig. 12), may have suppressed the northward component of oblique subduction resolved along the Cascadia subduction zone interface, thus transferring the northward component of strain into the upper plate and providing a plausible mechanism for the increase in north-south shortening within the backarc.

Finally, from seismic hazard assessment, we find that the interevent time between large magnitude earthquakes (M7–7.5), calculated from new slip rate and fault geometry estimates, ranges between 200 years and 6000 years. The relatively fast slip rate and long

length of the Umtanum Ridge anticline makes it one of the most potentially hazardous fault analyzed in the YFP.

## ACKNOWLEDGEMENTS

Funding for this research was awarded to L.M. Staisch through the USGS Mendenhall Postdoctoral Fellowship. We thank Julien Babault, Steve DeLong, and two anonymous reviewers for their comments on this manuscript. Their thorough attention and thoughtful comments improved the quality of our work. We would also like to thank Sean Gallen for informative and insightful discussions about geomorphic analyses, landscape evolution, and helpful tips on inversion methods. Any use of trade, firm, or product names is for descriptive purposes only and does not imply endorsement by the U.S. government. Non-proprietary LiDAR data are available from the Washington LiDAR Portal (<http://lidarportal.dnr.wa.gov/>). Additional data supporting the conclusions are either within the listed references or can be obtained in the supporting information. Supporting information is also available on ScienceBase (<https://www.sciencebase.gov/>).

## REFERENCES

- Audet, P., Bostock, M. G., Mercier, J.-P., & Cassidy, J. F. (2008). Morphology of the Explorer–Juan de Fuca slab edge in northern Cascadia: Imaging plate capture at a ridge-trench-transform triple junction. *Geology*, 36(11), 895–898. <https://doi.org/10.1130/G25356A.1>
- Bakun, W. H., Haugerud, R. A., Hopper, M. G., & Ludwin, R. S. (2002). The December 1872 Washington State Earthquake. *Bulletin of the Seismological Society of America*, 92(8), 3239–3258. <https://doi.org/10.1785/0120010274>
- Barry, T. L., Kelley, S. P., Reidel, S. P., Camp, V. E., Self, S., Jarboe, N. A., ... Renne, P. R. (2013). Eruption chronology of the Columbia River Basalt Group. In *Geological Society of America Special Papers* (Vol. 497, pp. 45–66). Geological Society of America. [https://doi.org/10.1130/2013.2497\(02\)](https://doi.org/10.1130/2013.2497(02))
- Bender, A. M., Amos, C. B., Bierman, P., Rood, D. H., Staisch, L., Kelsey, H., & Sherrod, B. (2016). Differential uplift and incision of the Yakima River terraces, central

Washington State. *Journal of Geophysical Research: Solid Earth*, 121(1), 365–384.  
<https://doi.org/10.1002/2015JB012303>

Benito, G., & O'Connor, J. E. (2003). Number and size of last-glacial Missoula floods in the Columbia River valley between the Pasco Basin, Washington, and Portland, Oregon. *Geological Society of America Bulletin*, 115(5), 624–638.

Bentley, R.D. (1977). Stratigraphy of the Yakima basalts and structural evolution of the Yakima ridges in the western Columbia Plateau, in Brown, E.H. and Ellis, R.C., editors, *Geological Excursions in the Pacific Northwest: Western Washington University*, p. 339-390. Published as a geology field guide in conjunction with the 1977 annual meeting of the Geological Society of America.

Blakely, R. J. (1995). *Potential theory in gravity and magnetic applications*. Cambridge University Press.

Blakely, R. J., Sherrod, B. L., Weaver, C. S., Wells, R. E., Rohay, A. C., Barnett, E. A., & Knepprath, N. E. (2011). Connecting the Yakima fold and thrust belt to active faults in the Puget Lowland, Washington. *Journal of Geophysical Research*, 116(B7).  
<https://doi.org/10.1029/2010JB008091>

Bretz, J. H. (1925). The Spokane Flood beyond the Channeled Scablands. II. *The Journal of Geology*, 33(3), 236–259. <https://doi.org/10.1086/623197>

Bretz, J. H. (1932). The Grand Coulee. *American Geographical Society Special Publication*, 15, 89.

Brown, B. H. (1937). The state-line earthquake at Milton and Walla Walla. *Bulletin of the Seismological Society of America*, 27(3), 205–209.

Camp, V. E. (1981). Geologic studies of the Columbia Plateau: Part II. Upper Miocene basalt distribution, reflecting source locations, tectonism, and drainage history in the Clearwater embayment, Idaho. *Geological Society of America Bulletin*, 92(9), 669–678.

Casale, G., & Pratt, T. L. (2015). Thin- or Thick- Skinned Faulting in the Yakima Fold and Thrust Belt (WA)? Constraints from Kinematic Modeling of the Saddle Mountains Anticline. *Bulletin of the Seismological Society of America*, 105(2A), 745–752.  
<https://doi.org/10.1785/0120140050>

Currie, C. A., Cassidy, J. F., & Hyndman, R. D. (2001). A regional study of shear wave splitting above the Cascadia Subduction Zone: Margin-parallel crustal stress. *Geophysical Research Letters*, 28(4), 659–662.

Czajkowski, J. L., Bowman, J. D., Schuster, J. E., & Wheeler, C. . (2012). *Oil and gas wells in Washington State* (Washington Division of Geology and Earth Resources Open File Report No. 2012-02).

DeLong, S. B., Hilley, G. E., Prentice, C. S., Crosby, C. J., & Yokelson, I. N. (2017). Geomorphology, denudation rates, and stream channel profiles reveal patterns of

mountain building adjacent to the San Andreas fault in northern California, USA. *Geological Society of America Bulletin*, 129(5–6), 732–749.

Doran, B. A. (2006). Structure of the Swauk basin and Teanaway dike swarm: Implications for basin inversion and Eocene extension in the central Cascades. In *Geological Society of America Abstracts with Programs* (Vol. 38, p. 5).

Dragovich, J. D., Logan, R. L., Schasse, H. W., Walsh, T. J., Lingley Jr, W. S., Norman, D. K., ... Meyers, K. D. (2002). Geologic map of Washington—Northwest quadrant. *Washington Division of Geology and Earth Resources Geologic Map GM-50*, 3. Retrieved from [https://gsa.confex.com/gsa/2002CD/finalprogram/abstract\\_35137.htm](https://gsa.confex.com/gsa/2002CD/finalprogram/abstract_35137.htm)

Eddy, M. P., Bowring, S. A., Umhoefer, P. J., Miller, R. B., McLean, N. M., & Donaghy, E. E. (2016). High-resolution temporal and stratigraphic record of Siletzia's accretion and triple junction migration from nonmarine sedimentary basins in central and western Washington. *Geological Society of America Bulletin*, 128(3-4), 425-441.

Evans, J. E. (1994). Depositional history of the Eocene Chumstick Formation: Implications of tectonic partitioning for the history of the Leavenworth and Entiat-Eagle Creek fault systems, Washington. *Tectonics*, 13(6), 1425–1444. <https://doi.org/10.1029/94TC01321>

Evans, J. E., & Johnson, S. Y. (1989). Paleogene strike-slip basins of central Washington: Swauk Formation and Chumstick Formation. *Washington Division of Geology and Earth Resources Information Circular*, 86, 215–237.

Finn, C., Phillips, W. M., & Williams, D. L. (1991). *Gravity anomaly and terrain maps of Washington* (USGS Numbered Series No. 988). Retrieved from <http://pubs.er.usgs.gov/publication/gp988>

Flint, J. J. (1974). Stream gradient as a function of order, magnitude, and discharge. *Water Resources Research*, 10(5), 969–973. <https://doi.org/10.1029/WR010i005p00969>

Fox, M., Leith, K., Bodin, T., Balco, G., & Shuster, D. L. (2015). Rate of fluvial incision in the Central Alps constrained through joint inversion of detrital <sup>10</sup>Be and thermochronometric data. *Earth and Planetary Science Letters*, 411, 27–36. <https://doi.org/10.1016/j.epsl.2014.11.038>

Fox, M., Goren, L., May, D. A., & Willett, S. D. (2014). Inversion of fluvial channels for paleorock uplift rates in Taiwan. *Journal of Geophysical Research: Earth Surface*, 119(9), 1853–1875. <https://doi.org/10.1002/2014JF003196>

Glotzbach, C. (2015). Deriving rock uplift histories from data-driven inversion of river profiles. *Geology*, 43(6), 467–470. <https://doi.org/10.1130/G36702.1>

Gomberg, J., Sherrod, B., Trautman, M., Burns, E., & Snyder, D. (2012). Contemporary Seismicity in and around the Yakima Fold-and-Thrust Belt in Eastern Washington. *Bulletin of the Seismological Society of America*, 102(1), 309–320. <https://doi.org/10.1785/0120110065>

Goren, L., Fox, M., & Willett, S. D. (2014). Tectonics from fluvial topography using formal linear inversion: Theory and applications to the Inyo Mountains, California. *Journal*

*of Geophysical Research: Earth Surface*, 119(8), 1651–1681.  
<https://doi.org/10.1002/2014JF003079>

Hack, J. T. (1957). Studies of longitudinal stream profiles in Virginia and Maryland. *US Geological Survey Professional Paper*, 294–B, 45–97.

Howard, A. D. (1994). A detachment-limited model of drainage basin evolution. *Water Resources Research*, 30(7), 2261–2285.

Howard, A. D., & Kerby, G. (1983). Channel changes in badlands. *GSA Bulletin*, 94(6), 739–752. [https://doi.org/10.1130/0016-7606\(1983\)94<739:CCIB>2.0.CO;2](https://doi.org/10.1130/0016-7606(1983)94<739:CCIB>2.0.CO;2)

Huffman, G.J., R.F. Adler, D.T. Bolvin, E.J. Nelkin, (2010). The TRMM Multi-satellite Precipitation Analysis (TMPA). Chapter 1 in *Satellite Rainfall Applications for Surface Hydrology*, F. Hossain and M. Gebremichael, Eds. Springer Verlag, ISBN: 978-90-481-2914-0, 3-22.

Hyndman, R. D., Riddihough, R. P., & Herzer, R. (1979). The Nootka Fault Zone — a new plate boundary off western Canada. *Geophysical Journal of the Royal Astronomical Society*, 58(3), 667–683. <https://doi.org/10.1111/j.1365-246X.1979.tb04801.x>

Johnson, S. Y. (1985). Eocene strike-slip faulting and nonmarine basin formation in Washington. *Society of Economic Paleontologists and Mineralogists Special Publication*, 37, 283–302.

Kelsey, H.M., Ladinsky, T.C., Staisch, L.M., Sherrod, B.L., Blakely, R.J., Pratt, T.L., Stephenson, W.J., Odum, J.K., Wan, E. (2017). The story of a Yakima fold and how it informs late Neogene and Quaternary backarc deformation in the Cascadia subduction Zone, Manastash anticline, Washington, USA. *Tectonics*, doi.10.1002/2017TC004558.

Kirby, E., Whipple, K., & Harkins, N. (2008). Topography reveals seismic hazard. *Nature Geoscience*, 1(8), 485.

Kirby, E., & Whipple, K. (2001). Quantifying differential rock-uplift rates via stream profile analysis. *Geology*, 29(5), 415–418.

Kirby, E., & Whipple, K. X. (2012). Expression of active tectonics in erosional landscapes. *Journal of Structural Geology*, 44, 54–75. <https://doi.org/10.1016/j.jsg.2012.07.009>

McCaffrey, R. (1992). Oblique Plate Convergence, Slip Vectors, and Forearc Deformation. *Journal of Geophysical Research*, 97(B6), 8905–8915.

McCaffrey, R. (2002). Crustal Block Rotations and Plate Coupling. *Plate Boundary Zones*, 101–119.

McCaffrey, R., King, R. W., Payne, S. J., & Lancaster, M. (2013). Active tectonics of northwestern U.S. inferred from GPS-derived surface velocities. *Journal of Geophysical Research: Solid Earth*, 118(2), 709–723.  
<https://doi.org/10.1029/2012JB009473>

- McCaffrey, R., King, R. W., Wells, R. E., Lancaster, M., & Miller, M. M. (2016). Contemporary deformation in the Yakima fold and thrust belt estimated with GPS. *Geophysical Journal International*, 207(1), 1–11. <https://doi.org/10.1093/gji/ggw252>
- Mendoza, M. K. (2008). Tectonic implications of the Eocene Teanaway dike swarm in the eastern Swauk basin, central Washington. In *Geological Society of America Abstracts with Programs*, 40(66).
- Miller, B. A. (2014). *On the origin of Umtanum Ridge: kinematics of Neogene slip* (Masters of Science). University of Washington, Seattle, Washington.
- Miller, R. B., Gordon, S. M., Bowring, S. A., Doran, B. A., McLean, N. M., Michels, Z. D., ... Mendoza, M. K. (2009). Linking deep and shallow crustal processes in an exhumed continental arc, North Cascades, Washington. *Field Guides*, 15, 373–406.
- Mullen, E. K., & Weis, D. (2015). Evidence for trench-parallel mantle flow in the northern Cascade Arc from basalt geochemistry. *Earth and Planetary Science Letters*, 414(Supplement C), 100–107. <https://doi.org/10.1016/j.epsl.2015.01.010>
- Nishimura, C., Wilson, D. S., & Hey, R. N. (1984). Pole of rotation analysis of present-day Juan de Fuca Plate motion. *Journal of Geophysical Research: Solid Earth*, 89(B12), 10283–10290. <https://doi.org/10.1029/JB089iB12p10283>
- Parker, R. L. (1994). *Geophysical Inverse Theory*, Princeton Univ. Press, Princeton, N. J.
- Perron, J. T., & Royden, L. (2013). An integral approach to bedrock river profile analysis. *Earth Surface Processes and Landforms*, 38(6), 570–576. <https://doi.org/10.1002/esp.3302>
- Porter, S.C. (1976). Pleistocene glaciation in the southern part of the Northern Cascade Range, Washington. *Geological Society of America Bulletin*, 87, 61–75.
- Pratt, T. L. (2012). Large-scale splay faults on a strike-slip fault system: The Yakima Folds, Washington State: Yakima Folds. *Geochemistry, Geophysics, Geosystems*, 13(11), n/a-n/a. <https://doi.org/10.1029/2012GC004405>
- Reidel, S. P. (1983). Stratigraphy and petrogenesis of the Grande Ronde Basalt from the deep canyon country of Washington, Oregon, and Idaho. *GSA Bulletin*, 94(4), 519–542. [https://doi.org/10.1130/0016-7606\(1983\)94<519:SAPOTG>2.0.CO;2](https://doi.org/10.1130/0016-7606(1983)94<519:SAPOTG>2.0.CO;2)
- Reidel, S. P., & Fecht, K. R. (1987). The Huntzinger flow: Evidence of surface mixing of the Columbia River Basalt and its petrogenetic implications. *Geological Society of America Bulletin*, 98(6), 664–677.
- Reidel, S. P., Camp, V. E., Tolan, T. L., & Martin, B. S. (2013). The Columbia River flood basalt province: Stratigraphy, areal extent, volume, and physical volcanology. *Geological Society of America Special Papers*, 497, 1–43.
- Reidel, S. P., Fecht, K. R., Hagood, M. C., & Tolan, T. L. (1989). The geologic evolution of the central Columbia Plateau. *Geological Society of America Special Papers*, 239, 247–264. <https://doi.org/10.1130/SPE239-p247>



- Riddihough, R. (1984). Recent Movements of the Juan de Fuca Plate System. *Journal of Geophysical Research*, 89(B8), 6980–6994.
- Rohr, K. M. M., & Furlong, K. P. (1995). Ephemeral plate tectonics at the Queen Charlotte triple junction. *Geology*, 23(11), 1035–1038. [https://doi.org/10.1130/0091-7613\(1995\)023<1035:EPTATQ>2.3.CO;2](https://doi.org/10.1130/0091-7613(1995)023<1035:EPTATQ>2.3.CO;2)
- Schuster, J. E. (1994). *Geologic map of the east half of the Yakima 1: 100,000 quadrangle, Washington*. Washington Division of Geology and Earth Resources.
- Smith, G. A., (1988a). Neogene synvolcanic and syntectonic sedimentation in central Washington, *Geological Society of America Bulletin*. 100, 1479-1492, doi: 10.1130/0016-7606(1988)100<1479:NSASSI>2.3.CO;2
- Smith, G. A. (1988b). Sedimentology of proximal to distal volcanoclastics dispersed across an active foldbelt: Ellensburg Formation (late Miocene), central Washington. *Sedimentology*, 35(6), 953–977.
- Smith, G. A. (1993). Missoula flood dynamics and magnitudes inferred from sedimentology of slack-water deposits on the Columbia Plateau, Washington. *Geological Society of America Bulletin*, 105(1), 77–100.
- Snyder, N. P., Whipple, K. X., Tucker, G. E., & Merritts, D. J. (2000). Landscape response to tectonic forcing: Digital elevation model analysis of stream profiles in the Mendocino triple junction region, northern California. *GSA Bulletin*, 112(8), 1250–1263. [https://doi.org/10.1130/0016-7606\(2000\)112<1250:LRTTFD>2.0.CO;2](https://doi.org/10.1130/0016-7606(2000)112<1250:LRTTFD>2.0.CO;2)
- Snyder, N. P., Whipple, K. X., Tucker, G. E., & Merritts, D. J. (2003). Importance of a stochastic distribution of floods and erosion thresholds in the bedrock river incision problem. *Journal of Geophysical Research: Solid Earth*, 108(B2), 2117. <https://doi.org/10.1029/2001JB001655>
- Staisch, L. M., Kelsey, H. M., Sherrod, B. L., Möller, A., Paces, J. B., Blakely, R. J., & Styron, R. H. (2017). Miocene–Pleistocene deformation of the Saddle Mountains: Implications for seismic hazard in central Washington, USA. *GSA Bulletin*, 129(X–X), X–X. <https://doi.org/10.1130/B31783.1>
- Swanson, D. A., Wright, T. L., Hooper, P. R., & Bentley, R. D. (1979). *Revisions in stratigraphic nomenclature of the Columbia River Basalt Group* (Bulletin No. 1457–G) (pp. G1–G59). US Geological Survey. Retrieved from <https://pubs.usgs.gov/bul/1457g/report.pdf>
- Tabor, R. W., Frizzell Jr, V. A., Vance, J. A., & Naeser, C. W. (1984). Ages and stratigraphy of lower and middle Tertiary sedimentary and volcanic rocks of the central Cascades, Washington: Application to the tectonic history of the Straight Creek fault. *Geological Society of America Bulletin*, 95, 26–44.
- Takeuchi, A. & Larson, P.B. (2005). Oxygen isotope evidence for the late Cenozoic development of an orographic rain shadow in eastern Washington, USA. *Geology*, 33(4), 313–316.

- Takeuchi, A., Hren, M.T., Smith, S.V., Chamberlain, C.P., Larson, P.B. (2010). Pedogenic carbonate carbon isotopic constrains on paleoprecipitation: Evolution of the desert in the Pacific Northwest, USA, in response to topographic development of the Cascade Range. *Chemical Geology*, 277, 323–335.
- Waitt, R. B. (1979), Late Cenozoic deposits, landforms, stratigraphy and tectonism in Kittitas Valley, Washington, U. S. Geological Survey Professional Paper 1127, 18 p. Available at <http://pubs.er.usgs.gov/publication/pp1127>
- Waitt, R. B. (1980). About Forty Last-Glacial Lake Missoula Jökulhlaups through Southern Washington. *The Journal of Geology*, 88(6), 653–679. <https://doi.org/10.1086/628553>
- Waitt, R. B. (1985). Case for periodic, colossal jökulhlaups from Pleistocene glacial Lake Missoula. *GSA Bulletin*, 96(10), 1271–1286. [https://doi.org/10.1130/0016-7606\(1985\)96<1271:CFPCJF>2.0.CO;2](https://doi.org/10.1130/0016-7606(1985)96<1271:CFPCJF>2.0.CO;2)
- Walsh, T. (1986). *Geologic map of the west half of the Yakima 1: 100,000 quadrangle, Washington*. Washington Division of Geology and Earth Resources.
- Wells, R. E., Weaver, C. S., & Blakely, R. J. (1998). Fore-arc migration in Cascadia and its neotectonic significance. *Geology*, 26(8), 759–762.
- Wells, R. E., & McCaffrey, R. (2013). Steady rotation of the Cascade arc. *Geology*, 41(9), 1027–1030. <https://doi.org/10.1130/G34514.1>
- West, M. W., Ashland, F. X., Busacca, A. J., Berger, G. W., & Shaffer, M. E. (1996). Late Quaternary deformation, Saddle Mountains anticline, south-central Washington. *Geology*, 24(12), 1123–1126.
- Wilson, M. S., Dyman, T. S., & Condon, S. M. (2008). Evaluation of well-test results and the potential for basin-center gas in the Columbia Basin, central Washington. In *Geologic Assessment of Undiscovered Gas Resources of the Eastern Oregon and Washington Province* (p. 12). Reston, VA: US Geological Survey.
- Whipple, K. X. (2004). Bedrock Rivers and the Geomorphology of Active Orogens. *Annual Review of Earth and Planetary Sciences*, 32(1), 151–185. <https://doi.org/10.1146/annurev.earth.32.101802.120356>
- Whipple, K. X., Hancock, G. S., & Anderson, R. S. (2000). River incision into bedrock: Mechanics and relative efficacy of plucking, abrasion, and cavitation. *Geological Society of America Bulletin*, 112(3), 490–503.
- Whipple, K. X., & Tucker, G. E. (1999). Dynamics of the stream-power river incision model: Implications for height limits of mountain ranges, landscape response timescales, and research needs. *Journal of Geophysical Research*, 104(B8), 17661–17674.
- Whittaker, A. C., Attal, M., Cowie, P. A., Tucker, G. E., & Roberts, G. (2008). Decoding temporal and spatial patterns of fault uplift using transient river long profiles. *Geomorphology*, 100(3), 506–526. <https://doi.org/10.1016/j.geomorph.2008.01.018>
- Wobus, C., Whipple, K. X., Kirby, E., Snyder, N., Johnson, J., Spyropolou, K., ... Sheehan, D. (2006). Tectonics from topography: Procedures, promise, and pitfalls. In *Special*



Accepted Article

*Paper 398: Tectonics, Climate, and Landscape Evolution* (Vol. 398, pp. 55–74).  
Geological Society of America. [https://doi.org/10.1130/2006.2398\(04\)](https://doi.org/10.1130/2006.2398(04))

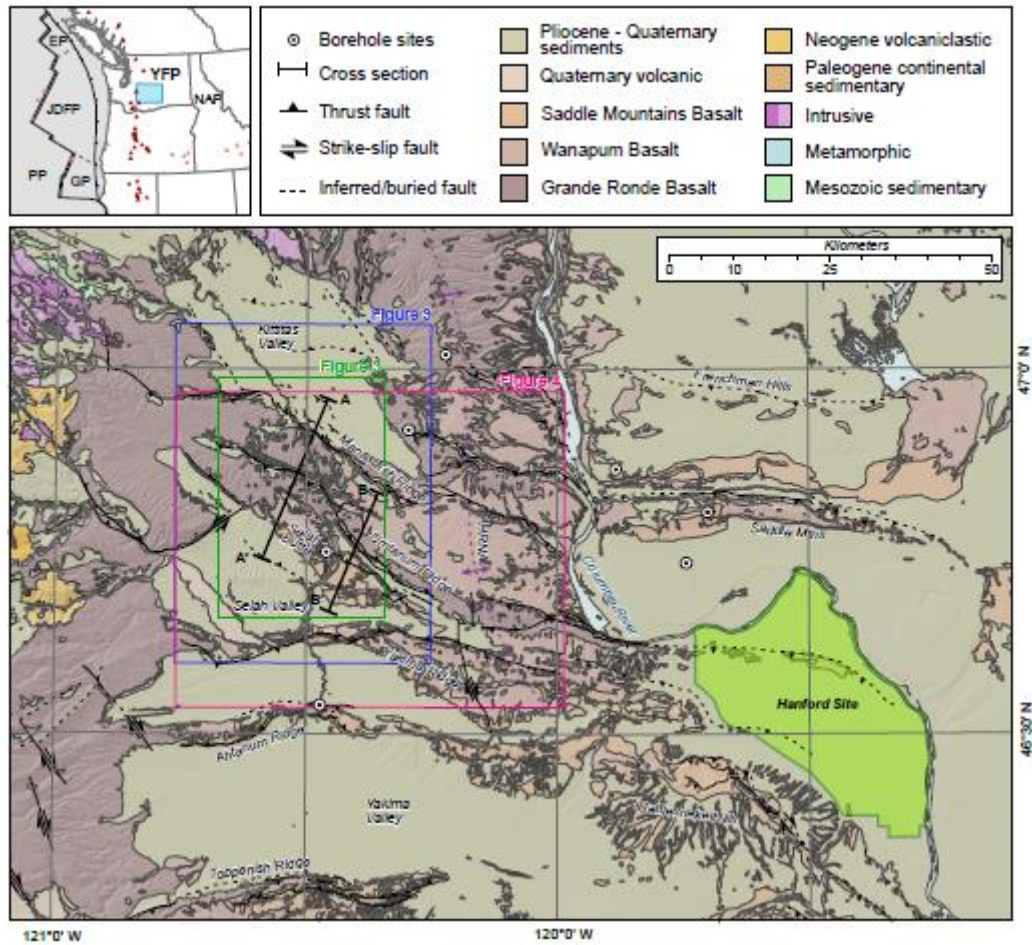


**Figure 1**

Geologic map of the Yakima Fold province simplified from the 1:250,000 scale map available at <http://www.dnr.wa.gov/geologyportal>. The underlying digital elevation model (DEM) hillshade derivative is 10 m resolution U.S. Geological Survey national map database ([ned.usgs.gov](http://ned.usgs.gov)). HRNA: Hog Ranch-Naneum anticline.

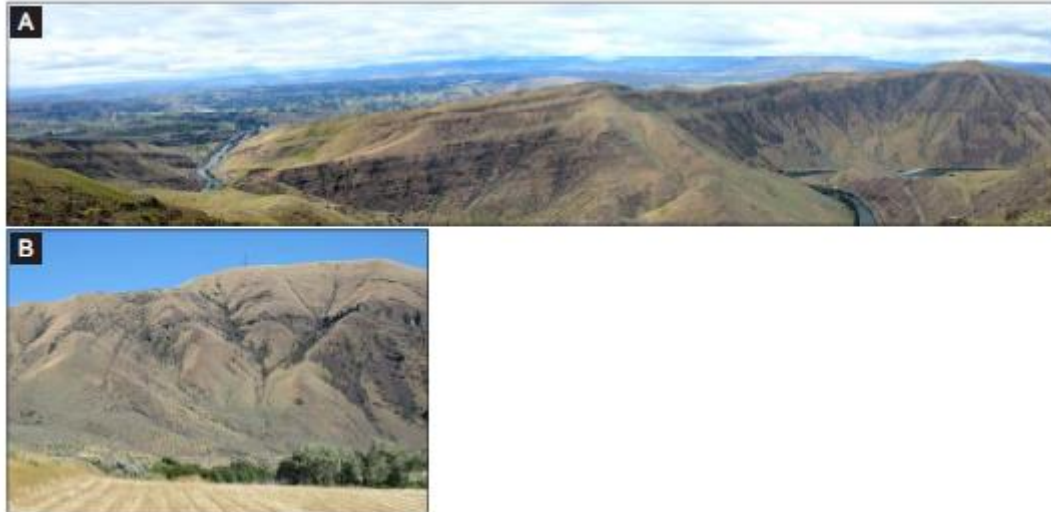


**Figure 2**

(A) Field photograph of the Yakima Canyon, taken from the crest of Selah Butte anticline on the east side of the Yakima River. Photo was taken facing southwest, looking into the Selah Valley. The Yakima Canyon incised ~600 m at this point and exposes stratigraphy from the Pomona member of the Saddle Mountains Basalt (top) to the R2 member of the Grande Ronde Basalt (bottom). Photo taken by L.M. Staisch. (B) Field photograph of the Umtanum Ridge anticline from the Yakima Canyon floor, looking southeast. Here, the Yakima River incises a deep cross section to show overturned basaltic strata of the north vergent Umtanum Ridge anticline. Photo by H.M. Kelsey.

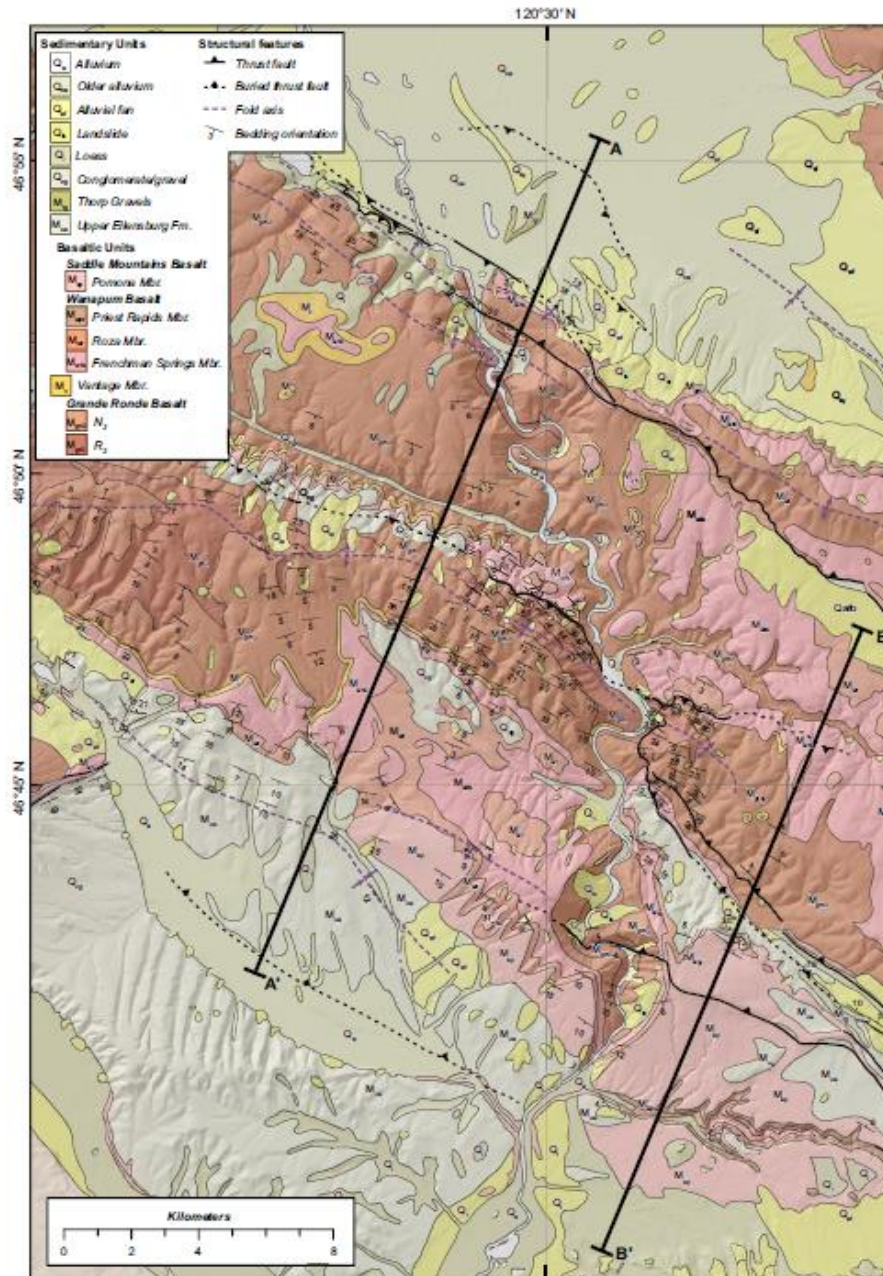


**Figure 3**

Detailed geologic map of the Yakima Canyon overlain on 2-m resolution LiDAR imagery. Geologic mapping is modified based on field and LiDAR observations from the 1:100,000 scale mapping (Schuster, 1994; Walsh, 1986) available at <http://www.dnr.wa.gov/geologyportal>. Mapped fault traces for the Manastash Ridge are adopted from Kelsey et al. (2017). Bedding orientations are sourced from Walsh, (1986), Schuster (1994) and Miller (2014).



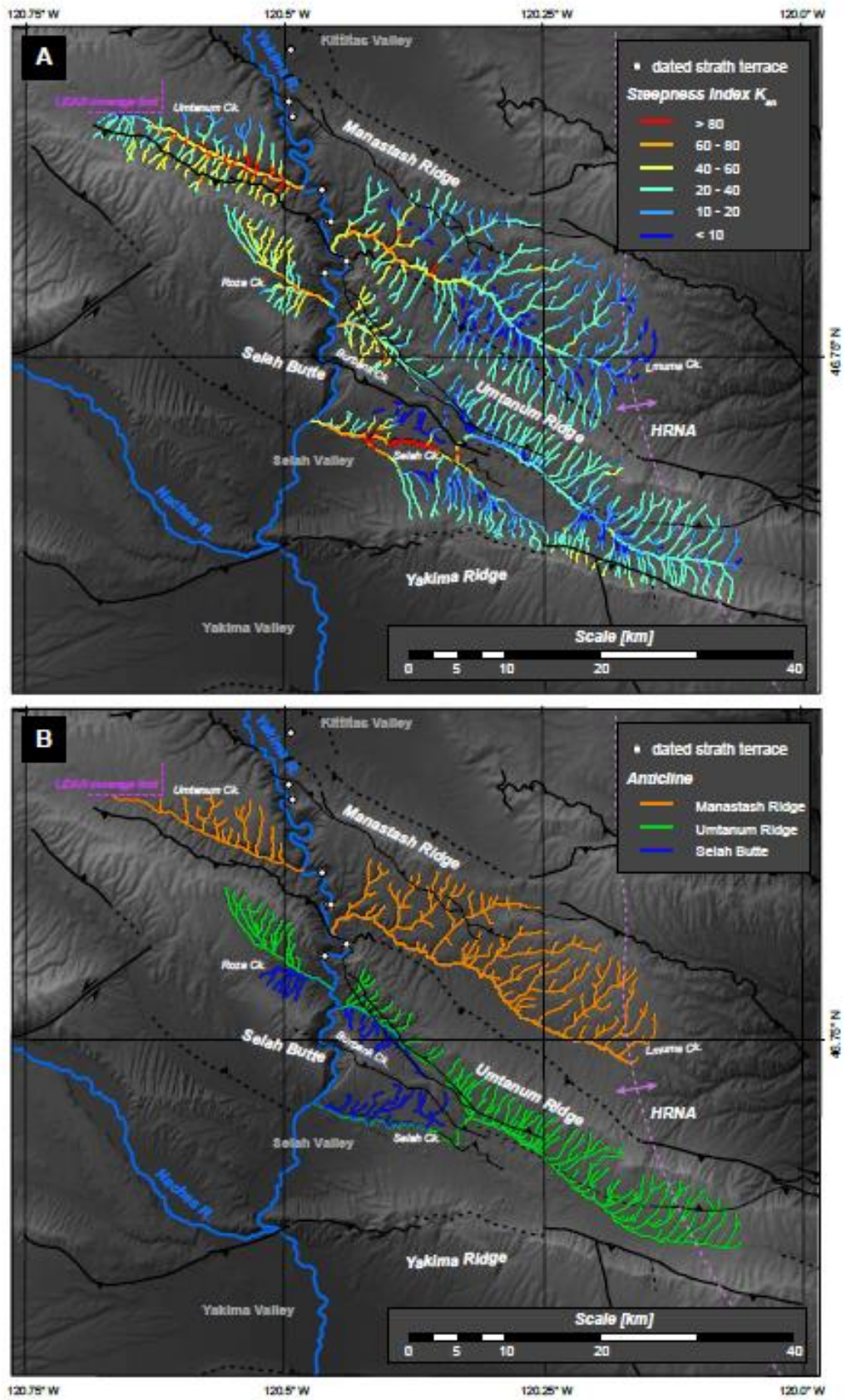


#### Figure 4

Geomorphic maps of the Yakima Canyon region. (A) Normalized channel steepness ( $k_{sn}$ ) is plotted for the streams extracted from 2-m resolution LiDAR data and analyzed, with warmer colors indicating higher  $k_{sn}$  values. Major changes in  $k_{sn}$  do not spatially correlate with mapped tectonic structures. (B) Streams selected for inversion and colored coded by the structure that they drain. For both maps, strath terraces dated by Bender et al. (2016) are plotted as white dots. DEM and hillshade derivative of the Yakima Canyon region are from LiDAR surveys where available (<http://lidarportal.dnr.wa.gov>), and 10 m resolution U.S. Geological Survey national map database ([ned.usgs.gov](http://ned.usgs.gov)). HRNA: Hog Ranch-Naneum anticline.

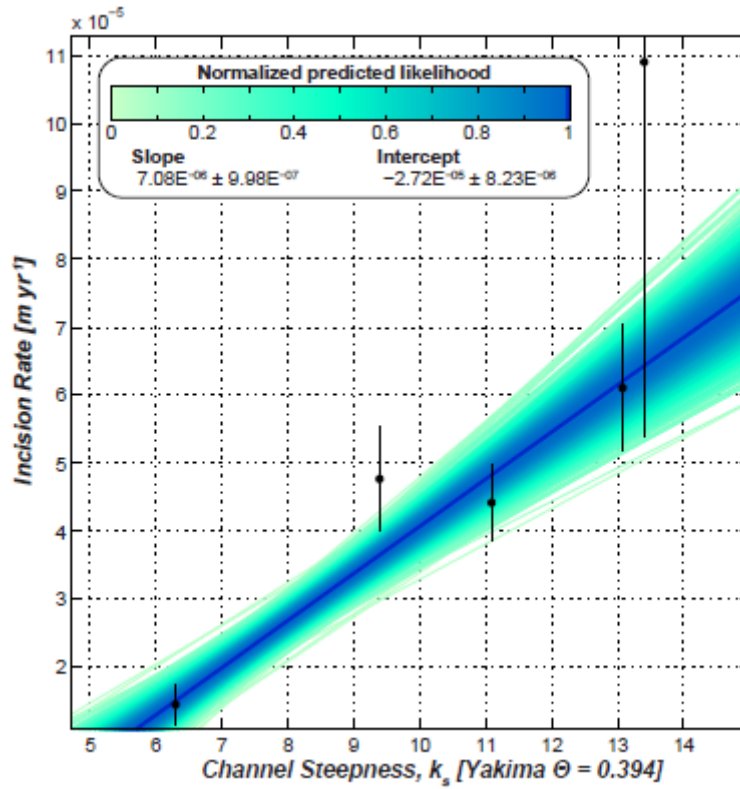


**Figure 5**

Incision rates measured from cosmogenically dated strath terraces (Bender et al., 2016) plotted against measured channel steepness values ( $k_s$ ) for along the Yakima River for each strath terrane location. The slope of the linear regression through these data points provides an estimate of the bedrock erodibility constant ( $K$ ).

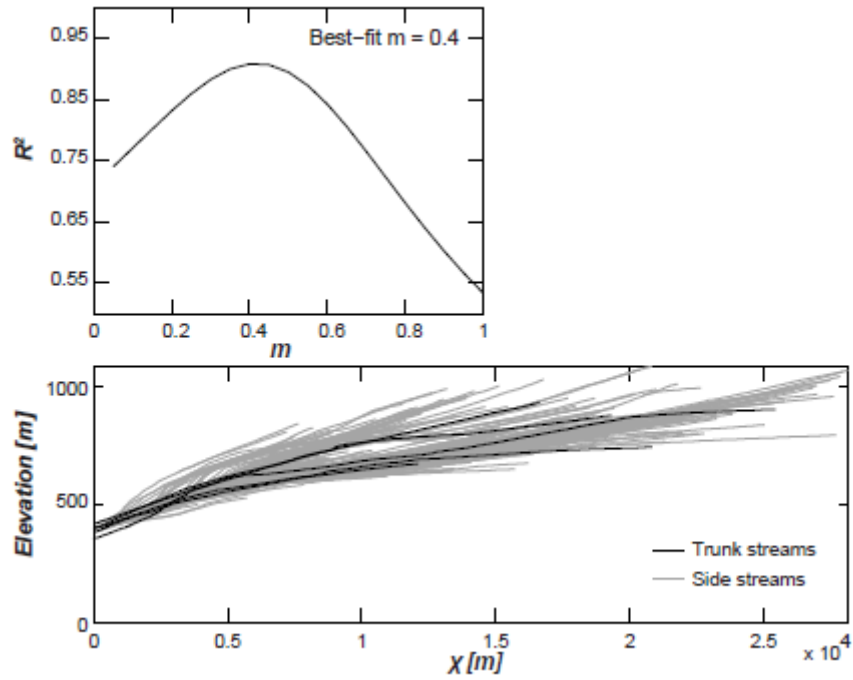


**Figure 6**

The upper plot shows the  $R^2$  value for linear regressions through  $\chi$ - $z$ , given a range in  $m$  values. The maximum  $R^2$  value obtained is when  $\chi$  is calculated with  $m=0.4$  for all streams. The lower plot is of  $\chi$  versus elevation ( $\chi$ - $z$  plot) for trunk streams (black) and side streams (grey) used in stream profile inversion, with  $m$  value set at its best-fit value of 0.4.



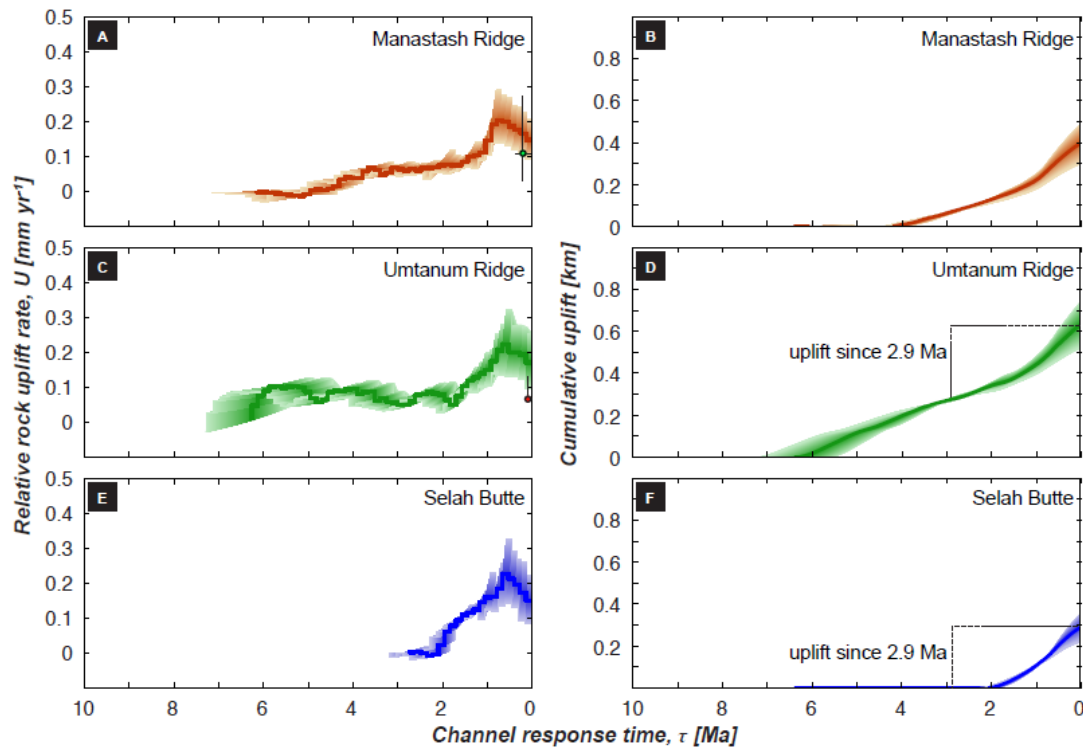


**Figure 7**

Results of stream profile inversion, plotted for each anticline as incision rate over time and cumulative uplift over time. Plots (A) and (B) are the incision rate and cumulative uplift, respectively, for the Manastash Ridge anticline. In (A), the incision rate measured from the Rattlesnake Dance terrace, near the crest of the Manastash Ridge anticline (Fig. 8), is plotted with uncertainty. Plots (C) and (D) are the incision rate and cumulative uplift, respectively, for the Umtanum Ridge anticline. In (C), the incision rate measured from the Big Pines terrace, near the crest of the Umtanum Ridge anticline (Fig. 8), is plotted with uncertainty. In (D), the amount of uplift measured from vertically offset 2.9 Ma Thorp Gravel deposits (Fig. 8) is plotted. Plots (E) and (F) are the incision rate and cumulative uplift, respectively, for the Selah Butte anticline.

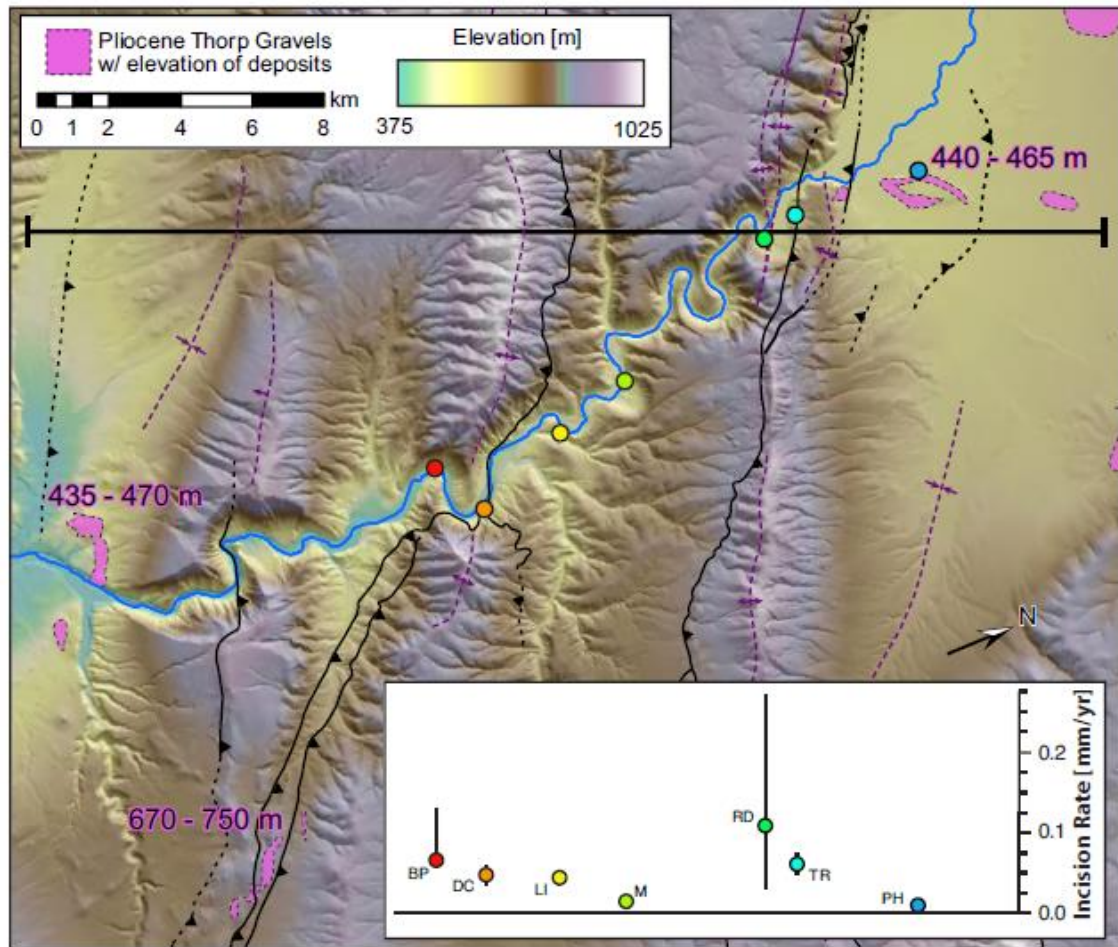


**Figure 8**

Topographic map of the Yakima Canyon, oriented with the inferred direction of maximum convergence as horizontal. Mapped deposits of the Pliocene Thorp Gravels are shown in pink, with their relative elevations noted in the Kittitas Valley, Selah Valley, and along the flanks of Umtanum Ridge. Dated strath terraces from Bender et al. (2016) are plotted as colorful dots, with associated calculated incision rates plotted on the inset graph. From left to right, strath terraces are BP: Big Pines, DC: Death Chute, LI: Lower Island, M: Meander, RD: Rattlesnake Dance, TR: Toth Road, and PH: Potato Hill.

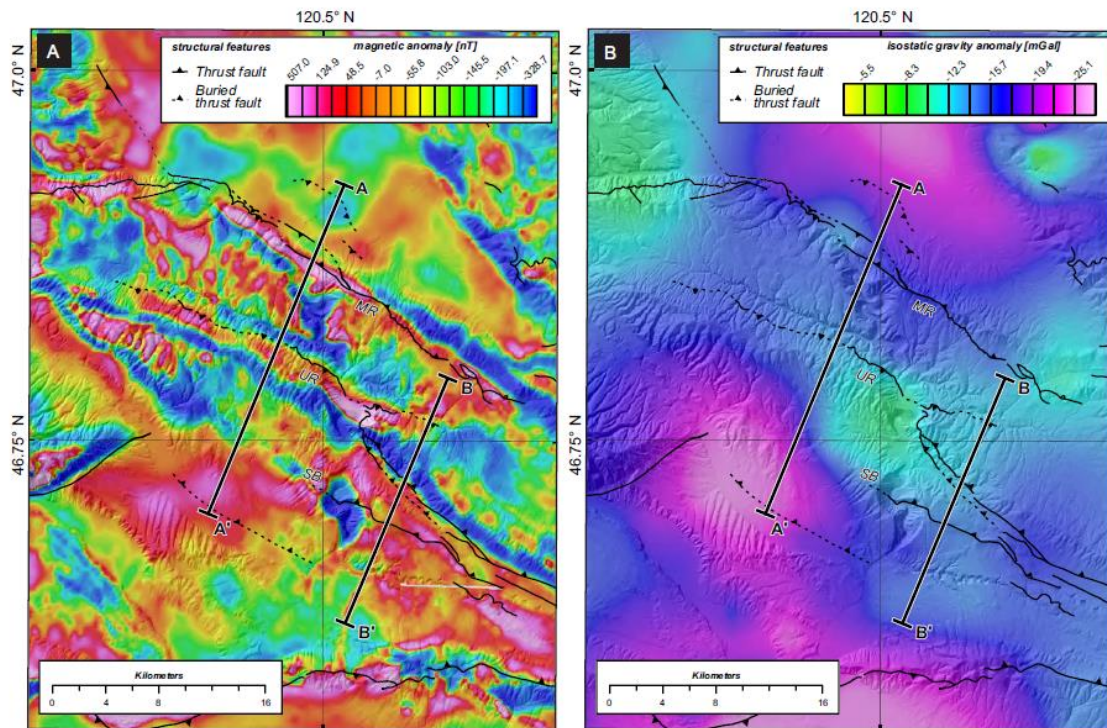


**Figure 9**

(A) Residual magnetic anomalies from high-resolution aeromagnetic data overlain on a hillshade map of the Yakima Canyon region. Fault traces are mapped in black, cross section transects and exploratory drill sites are plotted for reference. Magnetic anomaly data are extracted from the cross section transects and plotted in Figures 10A and 10E. (B) Isostatic residual gravity anomaly data is overlain over an otherwise identical map as (A). Gravity anomaly data are extracted from the cross section transects and plotted in Figures 10B and 10F. MR: Manastash Ridge, UR: Umtanum Ridge, SB: Selah Butte.

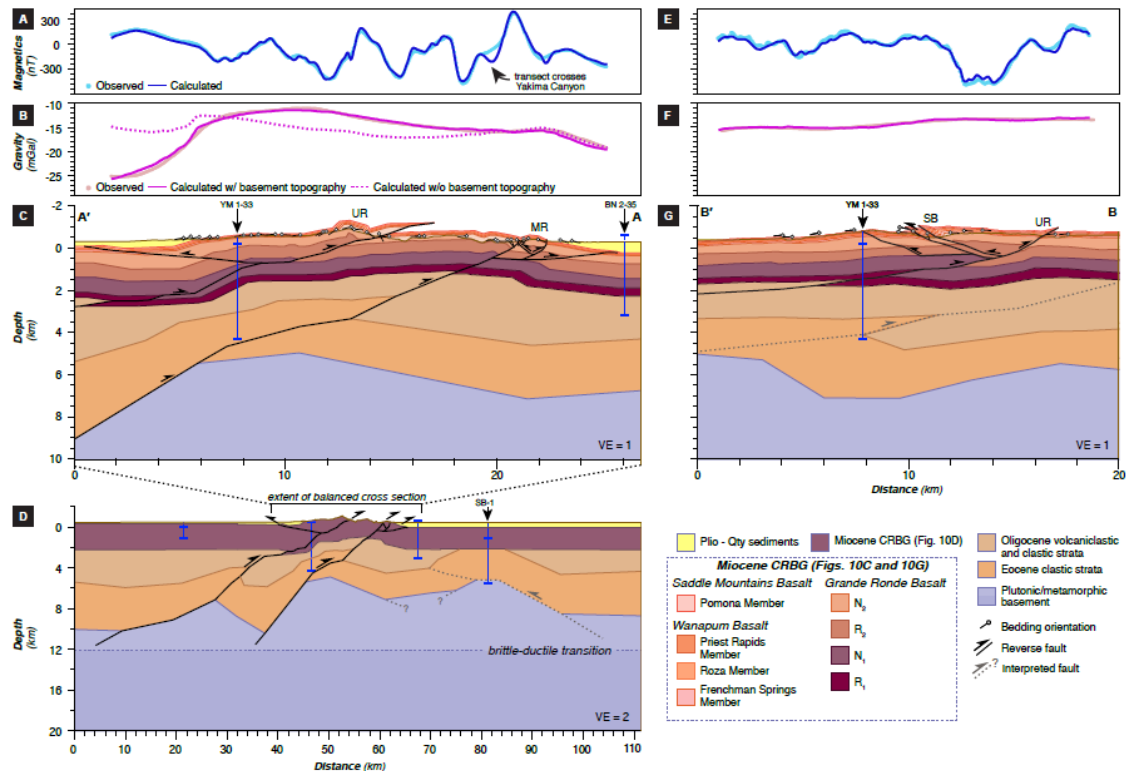


**Figure 10**

(A) Observed residual magnetic anomaly data extracted along A-A' shown in light blue. Forward-modeled magnetic anomalies are overlain in dark blue. (B) Observed isostatic residual gravity anomaly data extracted along A-A' shown in light pink. Modeled gravity anomalies with basement topography are shown as a solid dark pink line. The modeled gravity anomalies without basement topography (but the same upper crustal structure) are shown in the dotted pink line. (C) Cross section of the upper 10 km across the Manastash and Umtanum Ridge anticlines along A-A'. Dip ticks of structural measurements are plotted above the cross section. The location of exploratory drill sites YM 1-33 and BN 2-35 are shown in their projected location along the transect. YM 1-33 is located within the Yakima Canyon, and was drilled below the surface along A-A'. BN 2-35 is located along Boyleston Ridge and was drilled above the surface along A-A'. (D) An expanded view of the modeled basement topography required to fit measured gravity anomaly data in Figure 10B. The projected location of exploratory drill site SB-1, located northeast of the A-A', is shown.

Grey dashed faults in pre-Miocene strata and basement rocks are tentatively interpreted as structures that have little to no post-Miocene movement. (E) Observed residual magnetic anomaly data extracted along B-B' shown in light blue. Forward-modeled magnetic anomalies are overlain in dark blue. (F) Observed isostatic residual gravity anomaly data extracted along B-B' shown in light pink. Modeled gravity anomalies with basement topography are shown as a solid dark pink line. (G) Cross section of the upper 10 km across the Umtanum Ridge and Selah Butte anticlines along B-B'. Miocene CRBG strata are line balanced, whereas older strata that exhibit a prior history of deformation are not balanced. Dip ticks of structural measurements are plotted above the cross section and the location of exploratory drill site YM 1-33 is shown in its projected location along the transect. YM 1-33 is located within the Yakima Canyon, and was drilled below the surface along B-B'. MR: Manastash Ridge, UR: Umtanum Ridge, SB: Selah Butte.



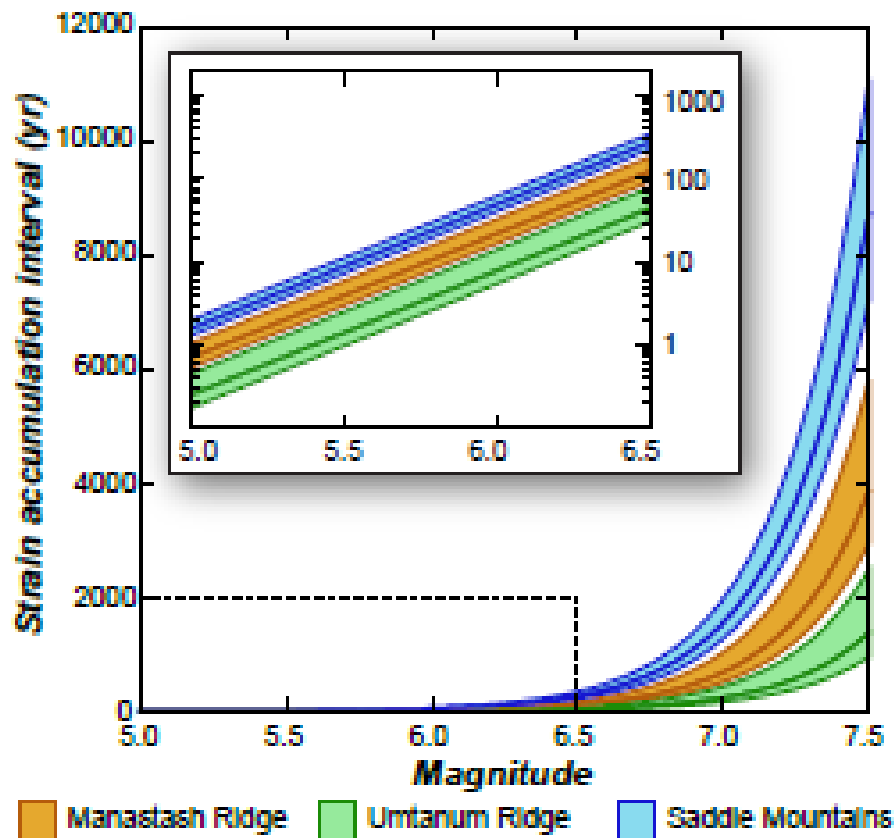


**Figure 11**

Estimates of the time required to accumulate sufficient strain energy along the faults that core the Umtanum Ridge, Manastash Ridge, and Saddle Mountains for earthquakes of given magnitude. The interevent timescale for earthquakes along the Saddle Mountains are given for the post-6.8 Ma slip rate (Staisch et al., 2017), are lower than the Manastash or Umtanum Ridge faults. However the results for the Saddle Mountains given a higher paleoseismic slip rate (West et al., 1996) are nearly identical to curves produced for the Manastash Ridge. Inset plot shows results for earthquake magnitudes between M5 – M6.5 on a logarithmic scale to emphasize the short time interval required.

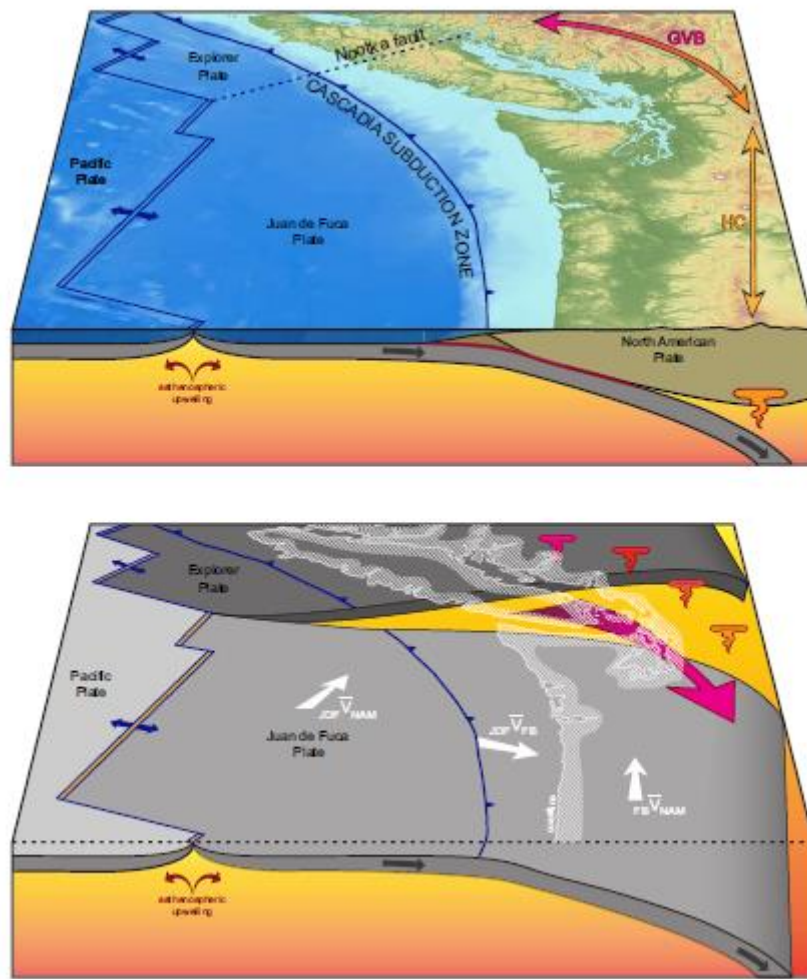


**Figure 12**

Block diagrams of the Cascadia subduction zone. (A) Diagram shows the location of the Garibaldi volcanic belt, where volcanic compositions are suggestive a northward increase in the component of primitive asthenospheric melt source. (B) Diagram with the upper plate stripped to show how a slab tear between the Explorer and Juan de Fuca plates may induce toroidal flow (large pink arrow) that inhibits the northward component of oblique subduction resolved along the Juan de Fuca – North America plate interface. Relative plate and crustal block velocities are shown in white.  $JDFV_{NAM}$  – Juan de Fuca velocity relative to North America.  $JDFV_{FB}$  – Juan de Fuca velocity relative to the forearc-backarc crustal block.  $FBV_{NAM}$  – forearc-backarc crustal block velocity relative to North America.



Table 1. Magnetic and density parameters used in forward models of gravity and magnetic anomalies.

<i>Unit</i>	$\rho$ g/cc	$\chi b$ emu/cc	<i>MR</i> <sub>c</sub> emu/cc	$\Delta\rho$ <sub>d</sub> g/cc
Pliocene - Quaternary strata	2.47	0.0000	0.0000	-0.20
Pomona Member - SMB	2.67	0.0005	-0.0025	0.00
Priest Rapids Member - WB	2.67	0.0005	-0.0025	0.00
Roza Member - WB	2.67	0.0005	-0.0025	0.00
Frenchman Springs Member - WB	2.67	0.0005	0.0025	0.00
Grande Ronde N2	2.67	0.0005	0.0025	0.00
Grande Ronde R2	2.72	0.0005	-0.0040	0.05
Grande Ronde N1	2.77	0.0005	0.0025	0.10
Grande Ronde R1	2.78	0.0005	-0.0025	0.11
Oligocene volcanoclastic strata	2.52	0.0000	0.0000	-0.15
Eocene clastic strata	2.62	0.0000	0.0000	-0.05
Basement	2.87	0.0000	0.0000	0.20
Lower crust	2.92	0.0000	0.0000	0.25

a SMB: Saddle Mountains Basalt; WB: Wanapum Basalt

b  $\chi$ : magnetic susceptibility

c MR = remanent magnetization

d  $\Delta\rho$ : density contrast relative to Bouguer reduction density (2.67 g/cc)

Table 2. Results of the rate and magnitude of deformation from stream profile inversion and cross section analyses.

Structure	<i>Stream Profile Inversion</i>		<i>Cross Section</i>		Fault Dip [°]	Slip Rate [mm/yr]
	Uplift Rate*	Cumulative Uplift	Shortening	Uplift†		
	[mm/yr]	[km]	[km]	[km]		
Manastash	$0.15 \pm 0.06$	$0.40 \pm 0.09$	1.10	0.50	24.3	$0.35 \pm 0.14$
Umtanum (A-A')	$0.17 \pm 0.09$	$0.63 \pm 0.11$	2.40	0.66	15.5	$0.64 \pm 0.34$
Umtanum (B-B')	$0.17 \pm 0.09$	$0.63 \pm 0.11$	1.64	0.65	20.1	$0.50 \pm 0.26$

\* values extracted stream profile results, averaged over the last 250 kyr, and reduced by 0.01 mm/yr to account for fluvial incision

† uplift calculated from the Yakima River to be consistent with stream profile inversion base level

Table 3. Parameters and results for estimating earthquake interevent times.

Structure	<i>Parameters</i>				<i>Results</i>	
	Slip Rate (s)	Fault length (L)	Seismic depth (z)	Fault Dip ( $\delta$ )	M7.0 Recurrence	M7.5 Recurrence
	[mm/yr]	[km]	[km]	[°]	[yrs]	[yrs]
Manastash fault	0.21 - 0.49	81	18.5	24.3	591 - 1378	3322 - 7752
Umtanum fault (A-A')	0.30 - 0.98	119	18.5	15.5	131 - 427	734 - 2398
Umtanum fault (B-B')	0.24 - 0.76	119	18.5	20.1	217 - 686	1218 - 3855
Saddle Mtns. fault (post Miocene)	0.15 - 0.23	116	18.5	37.0	1291 - 1971	7260 - 11082
Saddle Mtns. fault (Quaternary)	0.33 - 0.65	116	18.5	37.0	455 - 896	2557 - 5037